

*Parameterization of directional absorption of orographic gravity waves and its impact on the atmospheric general circulation simulated by the Weather Research and Forecasting Model*

Article

Accepted Version

Xu, X., Xue, M., Teixeira, M. A. C. ORCID: <https://orcid.org/0000-0003-1205-3233>, Tang, J. and Wang, Y. (2019) Parameterization of directional absorption of orographic gravity waves and its impact on the atmospheric general circulation simulated by the Weather Research and Forecasting Model. *Journal of the Atmospheric Sciences*, 76 (11). pp. 3435-3453. ISSN 1520-0469 doi: <https://doi.org/10.1175/JAS-D-18-0365.1> Available at <https://centaur.reading.ac.uk/85632/>

It is advisable to refer to the publisher's version if you intend to cite from the work. See [Guidance on citing](#).

To link to this article DOI: <http://dx.doi.org/10.1175/JAS-D-18-0365.1>

Publisher: American Meteorological Society

including copyright law. Copyright and IPR is retained by the creators or other copyright holders. Terms and conditions for use of this material are defined in the [End User Agreement](#).

[www.reading.ac.uk/centaur](http://www.reading.ac.uk/centaur)

## **CentAUR**

Central Archive at the University of Reading

Reading's research outputs online

1      **Parameterization of Directional Absorption of Orographic Gravity Waves and Its**  
2      **Impact on the Atmospheric General Circulation Simulated by the Weather**  
3      **Research and Forecasting Model**

4  
5  
6  
7      Xin Xu<sup>1</sup>, Ming Xue<sup>1,2</sup>, Miguel A. C. Teixeira<sup>3</sup>, Jianping Tang<sup>1</sup>, and Yuan Wang<sup>1</sup>  
8

9      <sup>1</sup> *Key Laboratory of Mesoscale Severe Weather/Ministry of Education and School of Atmospheric*  
10      *Sciences, Nanjing University, Nanjing 210023, Jiangsu, P. R. China*

11      <sup>2</sup> *Center for Analysis and Prediction of Storms, University of Oklahoma, Norman, OK 73072, USA*

12      <sup>3</sup> *Department of Meteorology, University of Reading, Earley Gate, PO Box 243, Reading RG6 6BB, UK*  
13  
14  
15  
16

17      Submitted to Journal of the Atmospheric Sciences  
18      20 Dec 2018  
19

20  
21      Revised April 6, July 25, 2019  
22  
23  
24  
25  
26

27      *Corresponding author*

28      Xin Xu

29      Key Laboratory of Mesoscale Severe Weather/Ministry of Education, and  
30      School of Atmospheric Sciences, Nanjing University

31      No. 163, Xianlin Avenue, Nanjing, Jiangsu, 210023, P. R. China

32      Email: xinxu@nju.edu.cn  
33  
34  
35

## Abstract

In this work, a new parameterization scheme is developed to account for the directional absorption of orographic gravity waves (OGWs) using elliptical mountain wave theory. The vertical momentum transport of OGWs is addressed separately for waves with different orientations through decomposition of the total wave momentum flux (WMF) into individual wave components. With the new scheme implemented in the Weather Research and Forecasting (WRF) model, the impact of directional absorption of OGWs on the general circulation in boreal winter is studied for the first time. The results show that directional absorption can change the vertical distribution of OGW forcing, while maintaining the total column-integrated forcing. In general, directional absorption inhibits wave breaking in the lower troposphere, producing weaker orographic gravity wave drag (OGWD) there and transporting more WMF upwards. This is because directional absorption can stabilize OGWs by reducing the local wave amplitude. Owing to the increased WMF from below, the OGWD in the upper troposphere at midlatitudes is enhanced. However, in the stratosphere of mid-to-high latitudes, the OGWD is still weakened due to greater directional absorption occurring there. Changes in the distribution of midlatitude OGW forcing are found to weaken the tropospheric jet locally and enhance the stratospheric polar night jet remotely. The latter occurs as the adiabatic warming (associated with the OGW-induced residual circulation) is increased at midlatitudes and suppressed at high latitudes, giving rise to stronger thermal contrast. Resolved waves are likely to contribute to the enhancement of polar stratospheric winds as well, because their upward propagation into the high-latitude stratosphere is suppressed.



## 1 Introduction

Mountains can generate gravity waves capable of transporting momentum upward from the troposphere to the middle atmosphere (Fritts and Alexander 2003; Alexander et al. 2010). Momentum transport by these orographically forced gravity waves (OGWs) or mountain waves has an important impact on the general circulation of the middle atmosphere where gravity waves tend to break. However, small-scale OGWs cannot be fully resolved by even high-resolution climate models like the Community Earth System Model (CESM, Hurrell et al. 2013). The effects of unresolved OGWs need to be parameterized in these models (Kim et al. 2003).

The parameterization of OGWs within numerical weather prediction (NWP) models dates back to the early 1980s. Palmer et al. (1986) and McFarlane (1987) established the first-generation OGW parameterization schemes according to the Eliassen-Palm (EP) flux theorem (Eliassen and Palm 1961) and the wave saturation hypothesis (Lindzen 1981). Later, these schemes were revised to better represent the momentum transport of gravity waves forced by large-amplitude mountains (Kim and Arakawa 1995; Lott and Miller 1997; Scinocca and McFarlane 2000; Webster et al. 2003). The major improvements were the inclusion of the effects of low-level wave breaking and flow blocking, which can respectively cause resonant amplification and reduction of gravity wave drag at the surface. Subgrid-scale orographic (SSO) properties, such as orographic asymmetry, convexity and anisotropy, were also considered (Kim and Doyle 2005).

The parameterization of OGWs is considered a necessary component in climate models given their relatively coarse horizontal resolutions. The parameterization can help reduce systematic model biases, such as the cold-pole bias associated with too strong westerlies in the mid and high latitudes, and delayed breakdown of the polar vortex in Antarctica (Palmer et al.

1986; Shin et al. 2010; McLandress et al. 2012; Pithan et al. 2016; Garcia et al., 2017; Garfinkel and Oman 2018). Furthermore, medium- and short-range weather predictions can also benefit from OGW parameterization (Hong et al. 2008; Zhong and Chen 2015; Choi and Hong 2015; Choi et al. 2017).

Like many other subgrid-scale processes however, gravity-wave drag is still not well represented in models. Biases in modelled atmospheric circulation that may result from an inaccurate representation of this drag are still a significant source of uncertainty in climate change projections (Shepherd 2014). According to the recent inter-comparison exercise proposed by the WMO Working Group for Numerical Experimentation (WGNE), parameterized orographic stresses have a considerable spread among models (Sandu et al. 2016). These large uncertainties have been attributed to the lack of observational constraints, so that parameters controlling the strength of OGWs are often tuned subjectively. A variational data assimilation technique was developed by Pulido and Thuburn (2005), aiming to estimate gravity wave forcing in the middle atmosphere and thus optimize parameterization. The parameters, although estimated for non-orographic gravity waves, have been shown to be helpful in simulating the splitting/breakup of the Antarctic polar vortex (Scheffler and Pulido, 2017).

Uncertainties of OGWs also result from misrepresentation of their physics in the model due to simplifying assumptions. For example, parameterized OGWs are assumed to propagate in the vertical only, but in reality they propagate both vertically and horizontally, i.e., they have a three-dimensional propagation (Alexander and Teitelbaum 2011; Kalisch et al. 2014; Ehard et al. 2017). Horizontal propagation of OGWs can reduce the local wave amplitude and thus affect wave breaking (Eckermann et al. 2015). Another process influencing the momentum transport of OGWs but missing in existing OGW parameterizations is the directional absorption (or, selective

critical-level absorption, Shutts 1995) of wave momentum flux (WMF). Hereafter, the term “WMF” will denote the momentum flux of subgrid-scale OGWs unless otherwise stated. In the case of mean flows turning with height (i.e., directionally sheared wind), there exist an infinite number of critical levels at different heights (Broad 1995) such that OGWs are continuously absorbed during propagation (Teixeira and Miranda 2009; Teixeira and Yu, 2014; Xu et al. 2012, 2013). Unlike the orographic gravity wave drag (OGWD), directional absorption of gravity waves exerts a lift force on the mean flow, i.e., an orographic gravity wave lift (OGWL), which is perpendicular to the mean flow (Xu et al. 2012).

Recently, Xu et al. (2018) designed an OGW parameterization scheme taking into account the directional absorption of OGWs (hereafter, the X18 scheme). *Offline* evaluation using reanalysis data in X18 showed that the scheme can produce weaker (stronger) OGWD in the lower stratosphere (upper stratosphere and lower mesosphere) because directional absorption tends to a transfer of wave breaking to higher levels. Although offline evaluation can provide some insights into the effects of directional absorption, it is yet unknown how this effect would affect large-scale circulations within actual numerical models. In principle, this can be examined by applying the X18 scheme within a numerical model that enables wave-mean flow interactions. However, the X18 scheme uses a high-order ray tracing method known as the Gaussian Beam Approximation (GBA, Pulido and Rodas 2011; Xu et al. 2017a). Although the GBA solution can be applied to OGWs forced by both idealized and realistic mountains, the wave fields are obtained by superposition of a number of Gaussians. This procedure is computationally very expensive, and hence limits its practical use for OGW parameterization within actual NWP or climate simulation models.

In this paper, a computationally more efficient parameterization scheme is proposed for the directional absorption of OGWs by assuming elliptically-shaped mountains. This assumption enables the use of analytical mountain wave solutions (Phillips 1984) within the parameterization scheme and removes the need for expensive ray tracing. Elliptical mountain wave theory has been used in previous OGW parameterization schemes (e.g., Lott and Miller 1997, hereafter LM97), yet the effect of directional absorption of OGWs, based on the theoretical approaches of Teixeira and Miranda (2009), Xu et al. (2012, 2013) and Teixeira and Yu (2014), was never considered. The scheme proposed in this work, which implements those approaches, is therefore used to revise the OGW parameterization scheme in the Weather Research and Forecasting (WRF) model, which was developed by Kim and Arakawa (1995, hereafter KA95) and Kim and Doyle (2005, hereafter KD05). With the original and revised parameterization schemes, global WRF simulations are conducted to examine the impact of directional absorption of OGWs on the large-scale atmospheric circulation.

This paper is organized as follows: Section 2 describes the new parameterization scheme and its implementation in the WRF model. The setup of numerical experiments performed using the WRF model is also introduced. In section 3, the effects of parameterized directional absorption on the vertical momentum transport of OGWs and large-scale atmospheric circulation are studied. A summary is given in section 4, including additional discussion.

## **2 Parameterization of OGWs in directionally sheared winds**

### **2.1 Theoretical framework**

Gravity waves forced by isolated obstacles are made up of wave components with different orientations. In current operational parameterization schemes, the ambient wind is

always assumed to be unidirectional, with all wave components treated as a whole for their upward propagation and breaking. In the case of winds with directional shear, different wave components are selectively filtered at different heights. Therefore, they should be addressed separately (see section 2.3 in Xu et al. 2018).

While there appears to be no simple way to represent the shape of the realistic SSO, previous schemes often assume an elliptical-shaped mountain of the form

$$h(x, y) = \frac{h_m}{\left[1 + \left(\frac{x}{a}\right)^2 + \left(\frac{y}{b}\right)^2\right]^\mu}, \quad (1)$$

where  $h_m$  is the mountain amplitude,  $a$  and  $b$  are the mountain half-widths in the  $x$  and  $y$  directions respectively, and  $\mu$  denotes the mountain sharpness. In this work,  $\mu$  is set to 3/2, for a bell-shaped mountain which has been widely used before (e.g., Teixeira and Miranda 2006). For hydrostatic and nonrotating airflow over an elliptical bell-shaped mountain, the WMF at the surface can be readily obtained according to linear wave theory

$$\boldsymbol{\tau}_0 = (\tau_x, \tau_y) = 0.5\rho_0 N |V_0| a h_m^2 \gamma \int_{-\pi/2}^{+\pi/2} (\cos\varphi, \sin\varphi) \cos(\varphi - \psi_0) [\gamma^2 \cos^2\varphi + \sin^2\varphi]^{-\frac{3}{2}} d\varphi, \quad (2)$$

where  $\rho_0$  is the Boussinesq flow base-state density,  $N$  is the Brunt-Väisälä frequency,  $|V_0|$  and  $\psi_0$  are the speed and direction of the horizontal wind at the surface,  $\gamma = \frac{a}{b}$  is the horizontal aspect ratio of the mountain, and  $\varphi$  is the azimuthal direction of the horizontal wave number. The detailed derivation of the above equation is given in the Appendix. It is important to notice that Eq. (2) is derived in a frame of reference aligned with the main axes of the elliptical mountain, i.e.,  $\tau_x$  and  $\tau_y$  are parallel to the two principal axes of the elliptical mountain respectively. For practical use in the OGW parameterization (such as its implementation in the WRF model

presented herein), this WMF needs to be remapped to the model coordinates by rotation of the coordinate system.

Assuming a simple case with  $\psi_0 = 0$ , i.e., the surface wind is along one of the principal axes of the elliptical mountain, the above equation reduces to

$$\tau_0 = 0.5\rho_0 N |V_0| a h_m^2 \int_{-\pi/2}^{+\pi/2} (\cos\varphi, \sin\varphi) F_{GW}(\varphi, \gamma) d\varphi, \quad (3)$$

$$F_{GW}(\varphi, \gamma) = \gamma \cos\varphi [\gamma^2 \cos^2\varphi + \sin^2\varphi]^{-\frac{3}{2}}. \quad (4)$$

In our implementation of this expression in the WRF OGWD parametrization scheme, to be tested for the first time in this paper, the above assumption is made. This is because in the KD05 OGWD scheme adopted in WRF the effective orography widths (i.e., the principal axes of the elliptical mountain) are only defined in the *along-wind* and in the *across-wind* direction (Fig. 1, see also Fig. 7 in KD05). Therefore, the low-level wind may be understood as being by definition along one of the mountain's principal axes. In the  $X'OY'$  coordinate defined by the mountain (Fig. 1), the total WMF at the surface ( $\tau_0$ ) is then simply in the  $x'$  direction, owing to the symmetry of the orography elevation. For any wave component  $\varphi_i$  in the azimuthal range  $(-\frac{\pi}{2}, +\frac{\pi}{2})$ , the corresponding WMF is along the direction of  $\varphi_i$  with its magnitude given by

$$|\tau_0(\varphi_i, \gamma)| = |\tau_0| \frac{F_{GW}(\varphi_i, \gamma)}{\int_{-\pi/2}^{+\pi/2} F_{GW}(\varphi, \gamma) d\varphi} = |\tau_0| R(\varphi_i, \gamma). \quad (5)$$

Evidently,  $R(\varphi_i, \gamma)$  only depends on the anisotropy of the assumed elliptical mountain. Thus for *practical use*, it is feasible to build a look-up table of  $R(\varphi, \gamma)$  for a number of discrete wave components at different orographic anisotropies. Figure 2 presents a few examples of  $R(\varphi, \gamma)$ . In the case with  $\gamma > 1$ , i.e., when the horizontal wind is parallel to the mountain ridge, the surface WMF is mainly represented by the along-wind wave components. By contrast, when the

horizontal wind is normal to the mountain ridge (i.e.,  $\gamma < 1$ ), the cross-wind wave components carry more WMF. For isotropic mountains with  $\gamma = 1$ ,  $R(\varphi, \gamma)$  is qualitatively similar to the case with  $\gamma > 1$  but the WMF is more evenly distributed about  $\varphi$ .

As mentioned above, in the presence of directional wind shear, the upward propagation and OGW momentum deposition should be addressed separately for different wave components. At each model level, the parameterization follows a two-step procedure.

(i) Directional absorption check. This is to remove the wave components (if any) from the wave packet which are selectively filtered between the current level and the level below. For example, the wave components between the azimuths of  $\varphi_1$  and  $\varphi_2$  are removed when the horizontal wind experiences a rotation from  $\mathbf{V}(z_1)$  to  $\mathbf{V}(z_2)$ , as shown in Fig. 1. The directionally absorbed waves produce a lift force (i.e., OGWL) pointing to the left (right) of a mean flow that backs (veers) with height (Xu et al. 2012);

(ii) Wave breaking check. This step is similar to that in previous parameterization schemes. The wave components not directionally filtered are taken as a whole. Airflow stability is checked according to the wave-modulated Richardson number  $Ri_m$ . If  $Ri_m$  falls below a critical value  $Ri_c$  (typically 0.25), wave breaking occurs and produces a drag force (i.e., OGWD) that is principally in the direction opposite to the flow, with the residual wave amplitude controlled by the saturation hypothesis.

The remaining WMF is passed on to the next model level, with the above procedure repeated until the WMF is totally attenuated or encounters the model top. Readers are referred to LM97 and KD05 for more details about this second step.

## 2.2 Implementation in WRF

The KD05 scheme in the WRF model actually includes two kinds of orographic drag, namely, flow blocking drag (FBD) and gravity wave drag. FBD occurs as the incident flow is blocked by the mountain when it does not have enough kinetic energy to go over it (LM97). In contrast, gravity wave drag is related to the breaking of vertically propagating OGWs which usually occurs at upper levels. For OGWs forced by large-amplitude mountains, this drag can also occur in the lower troposphere as a result of low-level wave breaking (KA95). In this study we mainly focus on the parameterization of gravity wave drag, including that due to directional wind shear which, as mentioned previously, we will call OGWL.

In the KD05 scheme, the WMF at the reference level (i.e., the effective mountain surface height in the model) is along the direction of the mean low-level wind, with its magnitude given by

$$\tau_{\text{ref}} = \rho_0 E \frac{m}{\lambda_{\text{eff}}} G \frac{|V_0|^3}{N}, \quad (6)$$

with

$$E = (OA + 2)^{C_E \frac{Fr_0}{Fr_c}}, m = (1 + L_x)^{OA+1}, G = \frac{Fr_0^2}{Fr_0^2 + C_G OC^{-1}}, \quad (7)$$

where  $E$  is the enhancement factor accounting for the drag enhancement by low-level breaking and/or lee wave trapping,  $m$  is the number of mountains within the model grid cell, and  $G$  is the asymptotic function providing a smooth transition between non-blocking and blocking flow. These parameters are controlled by both the incident flow properties and SSO statistics, e.g., orographic asymmetry (OA), orographic convexity (OC) and effective orographic length ( $L_x$ ) defined in the direction of the low-level wind (cf. Fig. 7 of KD05). The Froude number is given

by  $Fr_0 = \frac{Nh_m}{|V_0|} OD$  where  $OD = \frac{L_x^\perp}{L_x}$  is the orographic direction, with  $L_x^\perp$  the effective orography



length normal to  $L_x$ , i.e., in the cross-wind direction. Moreover,  $\lambda_{eff}$  is the effective grid length used as a tunable coefficient;  $C_E = 0.8$  and  $C_G = 0.5$  are constants calibrated according to mesoscale simulations (KA95). A critical Froude number of  $Fr_c = 1$  is used to determine the level of flow blocking.

Our new scheme can be readily implemented in the WRF model through modifications to the KD05 scheme. While one can readily obtain the magnitude of the surface WMF according to linear elliptical mountain wave theory, that quantity is simply set to  $\tau_{ref}$  in Eq. (6). This is to be compatible (and comparable) with the original scheme which also takes into account the effect of nonlinear mountain waves. The anisotropy of SSO is represented by  $OD$ , i.e.,  $\gamma = \frac{L_x}{L_x^\perp} = OD^{-1}$ . Given  $\tau_{ref}$  and  $R(\varphi_i, \gamma)$ , it is straightforward to obtain the reference-level WMF for each wave component. Note again that the wave components are in the coordinate system defined by the elliptical mountain, which should be rotated relative to the model coordinates. The upward transport of WMF in the KD05 scheme is also modified, following the above two-step procedure.

### 2.3 Setup of numerical experiments

Three sets of numerical experiments are conducted in this work by using the global version of the WRF model (GWRF). GWRF is an extension of the mesoscale WRF and a variant of Planet WRF (Richardson et al. 2007). Latitude-longitude horizontal coordinates are employed and Fourier spectral filtering is applied in the polar regions to avoid numerical instabilities near the poles. The first set of simulations is run without OGW parameterization (named CTL experiment), while the other two sets are run with the existing KD05 scheme (OLD experiment), and the revised scheme (NEW experiment). Each set consists of six simulations which are run from 00Z January 1 to 00Z February 1 from the year 2013 to 2018. The GWRF model is

configured with a horizontal resolution of  $1^\circ \times 1^\circ$  and 41 levels in the vertical, with the model top located at 10 hPa. Initial conditions come from the  $1^\circ \times 1^\circ$  Global Forecast System (GFS) analyses produced by the National Center for Environmental Prediction (NCEP). The available levels of the GFS data limit the choice of the WRF model top to 10 hPa. A sponge layer is placed at the top 5 km of the model domain, which aims to minimize the influence of waves reflected from the domain top. In this regard, only the numerical results below 20 hPa are studied in this work. The WRF single-moment 3-class scheme (Hong et al. 2004) is used for microphysics. Other model physics include the RRTMG longwave and shortwave radiation schemes (Iacono et al. 2008), the Yonsei University (YSU) Planetary Boundary Layer (PBL) scheme (Hong et al. 2006), the MM5 similarity scheme for the surface layer (Beljaars 1994), the new Tiedtke cumulus parameterization scheme (Zhang et al. 2011) and the Noah land surface model (Tewari et al. 2004).

### **3 Results**

#### **3.1 Zonal wind structure**

Figure 3a shows the zonal-mean zonal winds in January averaged over the six years from 2013 to 2018 from the  $2.5^\circ \times 2.5^\circ$  NCEP reanalysis (R2) in both the Southern and Northern Hemisphere (SH and NH). The most prominent features are the two tropospheric jets located in the subtropical upper troposphere. The NH tropospheric jet is more intense and occurs at higher altitude. Easterlies are found to prevail in the tropical lower-to-middle troposphere and SH stratosphere. Contrastingly, the NH stratosphere is dominated by westerlies, with another upper-level jet found in the high latitudes. This jet is actually the lower portion of the polar-night jet which is separated from the tropospheric jet.

Figures 3b-3d are the corresponding zonal-mean zonal winds obtained from the three experiments. In general, the WRF simulations can capture the structural features of the zonal winds well, including the two tropospheric jets and easterlies in the SH stratosphere. At first sight, the CTL experiment appears to best reproduce the zonal wind, for example, in terms of the maximum wind speed of the NH tropospheric jet. However, closer examination reveals that there are considerable discrepancies between the CTL simulation and reanalysis. As can be seen in Fig. 4a, westerly wind biases are found in the NH midlatitudes which extend vertically from the surface to the stratosphere. The largest bias occurs near 70 hPa, i.e., above the tropospheric jet. At both low and high latitudes, there are even stronger easterly wind biases, especially in the NH polar stratosphere where the negative wind biases exceed  $8 \text{ m s}^{-1}$ . By contrast, zonal winds in the SH are much better simulated than in the NH, with generally weaker biases (of less than  $3 \text{ m s}^{-1}$ ).

In the OLD experiment (Fig. 4b), the aforementioned westerly biases in NH midlatitudes are reduced significantly, showing little difference ( $< 1 \text{ m s}^{-1}$ ) from reanalysis. The deep column of positive bias at  $\sim 40^\circ\text{N}$  in CTL (Fig. 4a) is mostly gone (Fig. 4b). The zonal winds at low latitudes are also improved, although there are still notable biases in the upper troposphere. However, zonal winds are simulated worse at high latitudes, where the negative biases exceed  $10 \text{ m s}^{-1}$  in the stratosphere at  $\sim 60^\circ\text{N}$  (Fig. 4b). In the NEW experiment (Fig. 4c), the midlatitude westerly biases are also markedly reduced. The NH tropospheric jet intensity is slightly underestimated which, as will be shown later, is due to greater OGW forcing there. Nevertheless, there is an overall enhancement of stratospheric winds at high latitudes that reduces the negative biases compared to OLD (Fig. 4d). The negative biases in the high-latitude stratosphere are comparable to those in CTL (Figs. 4a, 4c), whereas the position of the polar night jet agrees

better with reanalysis (centered around  $65^{\circ}\text{N}$ , see Fig. 3). In this regard, among the three experiments the polar night jet is best reproduced in the NEW case.

Next, we will focus on the parameterized OGWs and their influence in the NH, because the SH is mainly covered by ocean, including few mountain ranges. Nonetheless, there is still strong OGW activity in the SH, especially during austral winter (Geller et al. 2013; Hindley et al. 2015), which has an important influence on the general circulation of the SH (McLandress et al. 2012). The effect of the revised parameterization scheme on the SH will be the object of a future study.

### 3.2 Distribution of WMF and OGW forcing in the NH

Figures 5a and 5b show the vertical distribution of zonal-mean WMF in the NH obtained from the OLD and NEW experiments, respectively. Similarly, Figs. 5c and 5d depict the vertical distribution of WMF normalized by the surface WMF. Significant WMF is found between  $30^{\circ}\text{N}$  and  $50^{\circ}\text{N}$  where the main mountain ranges exist in the NH, along with a secondary WMF maximum between about  $60^{\circ}\text{N}$  and  $70^{\circ}\text{N}$ . In the OLD and NEW experiments, the surface WMF is very similar because no changes were made to the reference-level WMF in the revised scheme. Accordingly, the column-integrated OGW forcing (or the total WMF divergence in the vertical column) in the two cases agree well with each other, with the largest forcing found in midlatitudes (Fig. 6). Hereafter, the total body force exerted on the mean flow by parameterized OGWs will be called OGW forcing unless explicitly stated. This is because OGWs in the NEW experiment produce both OGWD (by wave breaking) and OGWL (due to directional absorption) while there is only OGWD in the OLD case.

There are remarkable differences for the upward propagation of WMF. In the mid and high latitudes, on average more than 30% of the WMF originating at the surface can be

transported to the stratosphere, in particular between about  $45^{\circ}\text{N}$  and  $75^{\circ}\text{N}$ , which appears to be an atmospheric window for topographically forced gravity waves (Figs. 5c, 5d). This is because the steadily increasing wind speeds from the surface up to the polar-night jet at these latitudes allow for the vertical propagation of OGWs without encountering critical layers. The WMF in OLD decreases more rapidly with height than in NEW. Taking the WMF between  $45^{\circ}\text{N}$  and  $60^{\circ}\text{N}$  as an example, about 60% of the WMF is transported to above 100 hPa in the NEW experiment (Fig. 5d), while only  $\sim 40\%$  reaches that level in OLD (Fig. 5c). This means that the revised scheme allows more WMF to be transported to upper levels. In the latitudes south of about  $20^{\circ}\text{N}$ , the WMF generally cannot be transported to the stratosphere, showing a rapid drop by more than 80% in the upper troposphere. In the OLD case, this is due totally to wave breaking in the lower troposphere (Fig. 7a) where the zonal wind is reversed from easterlies to westerlies, forming a critical layer for OGWs (Booker and Bretherton 1967). In NEW, while low-level wave breaking still plays a dominant role (Fig. 7b), directional absorption of OGWs also makes a contribution, especially in the middle and upper troposphere (Fig. 7c).

In Fig. 7, wave attenuation at a given level is evaluated as the ratio between the attenuated WMF (due to either wave breaking or directional absorption) and the local WMF. As seen in Fig. 7c, directional absorption of OGWs is much weaker in midlatitudes than in low and high latitudes. This meridional variation largely depends on the rotation of the horizontal wind with height. As noted by Xu et al. (2012), the more the horizontal wind rotates with height, the more WMF is directionally absorbed. In winter, the rotation of tropospheric winds is weak in the midlatitudes of the NH (Xu et al. 2018), due to the strong westerly jet.

Given that the vertical gradient of WMF denotes the body force exerted on the mean flow by OGWs, the above results suggest different vertical distributions of total OGW forcing in the

two experiments. Figures 8a and 8b depict the zonal-mean zonal OGW forcing due to wave breaking (i.e., OGWD) in OLD and NEW respectively, with their difference (NEW minus OLD) shown in Fig. 8c. In both cases, significant OGWD is found in the lower troposphere as well as in the upper troposphere and stratosphere at midlatitudes, with the forcing maxima located just above the tropospheric jet core. There is a natural increase of OGWD with altitude due to the exponential reduction in air density, which results in an increase of wave amplitude. The weak winds in the lower stratosphere also favor breaking of mountain waves. This weak-wind layer has been named mountain-wave “valve layer” by Kruse and Smith (2016) since it controls the transport of wave momentum through it. Low-level OGWD is also found at low and high latitudes but is much weaker and less extensive than its midlatitude counterpart.

It is clear that the westerly biases in the midlatitudes of the CTL experiment are satisfactorily reduced because of the westward OGWD. However, there are apparent differences between the midlatitude OGWD in the two cases (Fig. 8c). The revised scheme generally produces weaker OGWD in the lower troposphere and stratosphere than the OLD experiment. On the contrary, OGWD is increased in the upper troposphere and lower stratosphere between about 200 hPa and 70 hPa. This behavior is closely related to the directional absorption of OGWs. As shown in Fig. 7, there is widespread suppression of wave breaking in the NEW experiment. For example, in the upper troposphere above the tropospheric jet, wave breaking in the OLD experiment causes attenuation of local WMF by up to 30%, while the WMF only attenuates by about 15% to 20% in the NEW experiment. This is because directional absorption is able to stabilize the OGWs by reducing the local wave amplitude. Due to such inhibition of wave breaking, there is a weakening of OGWD in the lower troposphere. But, at the same time, this allows more upward propagation of OGWs to the upper troposphere and stratosphere, as

evidenced by the greater WMF found there (Fig. 5). As such, the *upper-level* OGWD is determined by two opposite effects, i.e., the increased WMF which tends to enhance OGWD and directional absorption which is prone to suppress wave breaking and thus OGWD. In the upper troposphere, it is the former effect that dominates, giving rise to increased OGWD. By contrast, directional absorption has a larger impact in the stratosphere, with the stratospheric OGWD being in general decreased.

Meanwhile, considerable OGWL is produced in the stratosphere, showing a magnitude comparable to the OGWD difference (see Figs. 8c, 8d). As the zonal OGWL is mostly westward, it can to a certain degree compensate for the weakening of stratospheric OGWD. As seen in Fig. 8f, the total OGW forcing in the NEW experiment (i.e., sum of OGWD and OGWL, Fig. 8e) is strengthened in the stratosphere north of  $\sim 50^\circ\text{N}$ , compared to the OLD experiment (in which the total OGW forcing is simply the OGWD).

The zonal-mean meridional OGW forcing was also studied and shown to increase in the upper troposphere. Nonetheless, the meridional OGW forcing (not shown) is much weaker than its zonal counterpart.

### 3.3 Physical interpretation

The revised parameterization scheme produces more intense OGW forcing in the upper troposphere at midlatitudes, which correctly produces a weaker tropospheric jet in the NEW case. On the other hand, there is more notable enhancement of stratospheric winds at high latitudes (Fig. 4d), leading to a better representation of the polar night jet. What is responsible for the increase of polar stratospheric winds given the rather small direct OGW forcing found there?

Previous studies have showed that the momentum sink due to westward OGW forcing can induce a meridional circulation, with downward (upward) motion on the poleward (equatorward) flank of the forcing, which subsequently leads to adiabatic warming (cooling) (e.g., Palmer et al., 1986). The zonal mean temperature difference between OLD and CTL experiments (OLD minus CTL) is depicted in Fig 9a. There exists widespread warming in the upper troposphere of high latitudes (i.e., north of the maximum OGW forcing), with the warming center located near 65°N at 200 hPa. The meridional temperature gradient north of ~70°N is thus increased in the upper troposphere, which would enhance the stratospheric winds aloft according to the thermal wind relation. However, this effect appears to be largely cancelled out by the decrease of meridional temperature gradient in the stratosphere (i.e., cooling in midlatitudes and warming in polar regions). Stratospheric winds actually are decreased in OLD compared to the CTL experiment, leading to a worse simulation of the polar night jet. Figure 9b is similar to Fig. 9a but for the NEW experiment. Significant warming also occurs in the upper troposphere at mid and high latitudes. Compared to OLD, stronger warming is found between around 40°N and 60°N (Fig. 9c), in association with an equatorward displacement of the warming center to about 60°N, creating a larger gradient between the pole and ~60°N. Meanwhile, warming in the high latitudes north of about 70°N is suppressed in both the upper troposphere and stratosphere. Therefore, the meridional temperature gradient increases considerably in the polar region, resulting in stronger stratospheric winds than in CTL and OLD (Fig. 4).

In the above analysis, warming at high latitudes is attributed to the adiabatic sinking of the OGW-forced residual circulation. In accordance with the “downward control” principle (Haynes et al. 1991), the magnitude of the residual circulation (and hence of adiabatic warming) at a given level is proportional to the meridional gradient of OGW forcing above that level. For



the warming center existing at 200 hPa, Fig. 10a presents the integrated OGW forcing above 200 hPa for the OLD and NEW experiments, respectively, with their difference given in Fig. 10b. In the NEW experiment, the integrated OGW forcing is notably increased (i.e., more negative) between about 30°N and 40°N, primarily owing to its enhancement in the upper troposphere (Fig. 8f). Meanwhile, a relatively small reduction is found between about 42°N and 52°N, in response to the weakened stratospheric OGW forcing. In consequence, the meridional gradient of integrated OGW forcing is enhanced between about 30°N and 50°N, giving rise to the intensified warming found in Fig. 9c. Similarly, the suppression of warming at high latitudes can be ascribed to the decreased meridional gradient of integrated OGW forcing between about 50°N and 60°N. The integrated OGW forcing above 50 hPa was also studied. It is mainly decreased between about 25°N and 45°N but increased poleward (not shown), causing a decrease of warming in the stratosphere at high latitudes.

Besides parameterized OGW forcing, the zonal winds in the stratosphere at high latitudes can also be affected by resolved waves, for example, vertically propagating Rossby waves (e.g., McLandress and Shepherd 2009). The modification of the large-scale flow by parameterized OGWs can influence the propagation of resolved waves and thus their forcing (McLandress et al. 2012; Sandu et al. 2016; van Niekerk et al. 2017). Indeed, previous studies have suggested a compensation between parametrized and resolved wave drag in the stratosphere (e.g., Cohen et al. 2013; Sigmond and Shepherd 2014). Resolved-wave forcing (which may include both Rossby waves and resolved inertia-gravity waves) can be quantified by the divergence of their EP flux (Andrews 1987). Following Edmon et al. (1980), the zonal-mean EP flux associated with resolved waves was calculated and is shown in Fig. 11 for the OLD and NEW experiments respectively. Resolved waves are found to propagate upward from the lower troposphere at

midlatitudes and separate into two branches in the upper troposphere, with one branch propagating equatorward and the other propagating upward into the stratosphere (Figs. 11a, 11b). The latter branch appears to diverge above about 100 hPa, showing both equatorward and poleward propagations. Nonetheless, the westward resolved-wave forcing in the stratosphere (i.e., EP flux convergence) indicates that the horizontal divergence of EP flux is overwhelmed by vertical convergence there. In the NEW case, the vertical propagation of resolved waves is reduced, yielding weaker resolved wave forcing in the high-latitude stratosphere (Fig. 11c). Thus the resolved wave forcing may also act to produce stronger polar stratospheric winds in the NEW experiment, although the difference between the resolved wave forcings of the two experiments is not significant at the 99% level (not shown).

#### **4. Discussion and conclusions**

Internal gravity waves forced by mountains have long been considered an important process in the coupling between the lower troposphere and middle atmosphere, given their ability to transport momentum from source regions at the surface to the upper levels where the waves break. Vertical momentum transport by orographic gravity waves (OGWs) is affected by directional shear of the mean flow, which is known as directional wave absorption. In such a case, OGWs can produce a lateral lift force (i.e., OGWL) on the mean flow, in addition to the commonly-known orographic gravity wave drag (OGWD) induced by wave breaking. However, this effect is not considered in existing OGW parameterization schemes (at least operational ones), and it is an important source of error in subgrid-scale OGW parameterization.

In this study, a new parameterization scheme is developed which explicitly deals with the directional absorption of OGWs. By assuming an elliptical shape for subgrid-scale orography, the wave momentum flux (WMF) carried by each wave component can be easily obtained by

using elliptical mountain wave theory (Phillips 1984). Therefore, the new scheme is computationally efficient and acts only within the vertical column, meaning it could be easily adopted operationally. Nonetheless, since the momentum transport by each wave component is handled separately in the new scheme, this increases the computational cost depending on the number of wave components used. In the current study we use 60 wave components evenly distributed in the azimuthal angle interval  $(-\pi/2, \pi/2)$ , leading to  $\sim 30\%$  more CPU time. The vertical propagation and momentum deposition of different wave components is handled separately (rather than as a full spectrum, as is the case with normal OGWD that does not consider directional absorption). The new scheme is implemented in the WRF model, as an addition to the existing OGW drag parameterization scheme, to investigate the impact of parameterized directional absorption of OGWs on the general atmospheric circulation. Three sets of numerical experiments are conducted, containing six one-month-long global simulations from January 2013 to 2018. The first experiment, CTL, is run without an OGW parameterization. The other two experiments separately employ the original OGWD parameterization scheme of KD05 and the improved scheme proposed herein, i.e., the OLD and NEW experiments, respectively.

The structure of the simulated zonal wind is compared with the NCEP reanalysis data (R2). The CTL experiment shows pronounced westerly wind biases in the midlatitudes of the Northern Hemisphere (NH), with salient easterly wind biases present in the low-latitude troposphere and high-latitude stratosphere. On the contrary, the zonal wind structure in the Southern Hemisphere (SH) is much better reproduced and, moreover, is less sensitive to the parameterization of OGWs. In the OLD experiment, the westerly biases in midlatitudes are significantly reduced, due to the presence of OGW forcing there. The simulated tropospheric jet is brought to a good agreement with reanalysis. The NEW experiment also achieves a

satisfactory reduction of midlatitude westerly biases, although the tropospheric jet is slightly underestimated because of the stronger OGW forcing in the upper troposphere at midlatitudes. On the other hand, the stratospheric winds at high latitudes are simulated worse in the OLD experiment, whereas there is an overall enhancement in NEW, with the stratospheric polar night jet being best reproduced among the three experiments.

The vertical momentum transport of OGWs and the resulting OGW forcing are studied, with particular attention paid to the NH midlatitudes, where the strongest orographic forcing is present. The OLD and NEW experiments show very similar surface WMF and column-integrated OGW forcings, but the vertical distributions of the OGW forcing are quite different, which is caused by the directional absorption of OGWs. The directional absorption has a tendency to inhibit wave breaking, producing weaker OGWD in the lower troposphere. On the other hand, the suppressed low-level wave breaking allows for more upward transport of WMF to the upper troposphere and stratosphere, which can induce stronger OGWD there via wave breaking. Therefore, the upper-level OGWD is jointly determined by two competing effects, i.e., increased WMF from below and local directional absorption. In the upper troposphere, the former effect dominates, thus increasing the OGWD above the tropospheric jet. Conversely, this effect is overwhelmed by the enhanced directional absorption in the stratosphere at mid-to-high latitudes, with the OGWD being reduced there. Nevertheless, the total OGW forcing (i.e., sum of OGWD and OGWL) in NEW is still improved in the stratosphere north of  $\sim 50^\circ\text{N}$ , because the weakened stratospheric OGWD is compensated by the considerable OGWL present there.

It is noteworthy that the OGWL studied in this work is different from the mountain lift mentioned by Lott (1999). The latter is a lateral force exerted by the subgrid-scale orography caused by the pressure gradient associated with geostrophic balance of the incoming flow. It is

therefore proportional to the Coriolis parameter. This mountain lift associated with the Earth's rotation can significantly affect the pattern of steady Rossby waves (Lott 1999). Conversely, the OGWL discussed herein is the same as that studied in Martin and Lott (2007), which can cause synoptic-scale disturbances.

Possible links between the changes of midlatitude OGW forcing and stratospheric winds at high latitudes are explored, which are summarized schematically in Fig. 12. In the NEW experiment, the increased OGW forcing in the midlatitude upper troposphere and more widespread weakening of stratospheric OGW forcing jointly enhance upper-tropospheric adiabatic warming (associated with the wave-induced vertical residual circulation) between about 40°N and 60°N. Meanwhile, adiabatic warming is suppressed in the upper troposphere and stratosphere at high latitudes north of ~70°N, due mainly to the reduced stratospheric OGW forcing. Such changes enhance the meridional temperature gradient at high latitudes, which in turn strengthens the polar stratospheric winds according to the thermal wind relation. In addition to parameterized OGWs, the role played by resolved waves is also addressed. In the NEW experiment, there is an increase of equatorward propagation of EP flux in the upper troposphere, whereas the vertical propagation of resolved waves is reduced, leading to a weakening of resolved-wave forcing in the stratosphere. This might also contribute to the intensification of stratospheric winds. Nonetheless, the relative importance of parameterized and resolved wave forcing requires further quantitative diagnostic study.

The result that directional absorption can redistribute the OGW forcing and affect the large-scale circulation both directly and indirectly seems to be rather robust. An additional sensitivity experiment (NEW1) was conducted, similar to NEW but with the directional absorption of OGWs included only above the PBL. This can be viewed as a case with “weak

directional absorption”, as it omits the rotation of the horizontal wind within the boundary layer. The results in NEW1 are qualitatively similar to those in NEW but show weaker differences in the zonal winds, OGW forcing, etc. (Figs. 13, 14), consistent with the weaker effect of directional absorption of OGWs. This suggests an interaction between parameterized OGWs and the PBL (Kim and Hong 2009).

For the implementation of the new scheme in the WRF model, the low-level wind is assumed to be aligned with one of the principal axes of the elliptical mountain. The main reason for considering only this incidence angle is to be consistent with the KD05 scheme within WRF, which is extended in this study to include the additional effect of directional absorption. In the LM97 scheme, which also uses elliptical mountain wave theory, the incoming flow can be oblique to the principal axes of the mountain, allowing a misalignment between surface WMF and wind. Further development is needed to relax the former assumption, which will be a topic for future research.

The propagation of resolved waves and their forcing are influenced by the modification of the large-scale circulation. This is one component of the problem of the complicated interactions involving parameterized wave drag, resolved wave drag and mean flow, which has important implications for both present-day climate and projections of future climate change (McLandress and Shepherd 2009; Sigmond and Scinocca 2010; Calvo et al. 2017) as well as for NWP. As shown by Smith et al. (2017), the variability of the troposphere can be transported to the mesosphere and lower thermosphere by gravity waves. Given the limitation that the model top is at 10 hPa in the present study, it is not possible to know how directional absorption of OGWs will affect the general circulation in the middle atmosphere. According to Xu et al. (2018), the OGWD in the upper stratosphere and lower mesosphere are in general increased

548 under the influence of directional absorption of OGWs. This will be studied in more detail in the  
549 future by implementing the new scheme in a more comprehensive climate model.

550

551 *Acknowledgments.* The authors would like to thank the anonymous reviewers for their comments.

552 This study is mainly supported by the National Science Foundation of China (Grants 91837207,

553 41875068, 41505046).

## Appendix A: Derivation of surface WMF of OGWs forced by elliptical mountains

For linear mountain waves, the momentum flux at the surface  $\tau_0$  is given by

$$\tau_0 = -\rho_0 \int_{-\infty}^{+\infty} \int_{-\infty}^{+\infty} \mathbf{v}_0' w_0' dx dy, \quad (\text{A1})$$

where  $\mathbf{v}_0' = (u', v')$  and  $w_0'$  are the horizontal and vertical velocity perturbations of gravity waves at the surface. Using two-dimensional Fourier transforms, i.e.,

$$A'(x, y, z) = \int_{-\infty}^{+\infty} \int_{-\infty}^{+\infty} \hat{A}(k, l, z) e^{i(kx+ly)} dk dl, \quad (\text{A2})$$

$$\hat{A}(k, l, z) = \frac{1}{4\pi^2} \int_{-\infty}^{+\infty} \int_{-\infty}^{+\infty} A'(x, y, z) e^{-i(kx+ly)} dx dy, \quad (\text{A3})$$

with  $A'(x, y, z)$  and  $\hat{A}(k, l, z)$  being a generic field in physical and spectral space, respectively, Eq. (A1) can be written as

$$\tau_0 = -4\pi^2 \rho_0 \int_{-\infty}^{+\infty} \int_{-\infty}^{+\infty} \hat{\mathbf{v}}_0' \hat{w}_0^* dk dl, \quad (\text{A4})$$

where  $\hat{w}_0^*$  is the complex conjugate of  $\hat{w}_0$  and  $k$  and  $l$  are the components of the horizontal wavenumber vector  $\mathbf{K} = (k, l)$ .

In a situation of spatially uniform hydrostatic flow past an isolated obstacle, the vertical velocity in spectral space can be easily obtained by solving the Taylor-Goldstein equation (cf. Eq. (9) in Xu et al., 2012), yielding

$$\hat{w} = i(Uk + Vl) \hat{h} e^{\frac{NK}{Uk+Vl}z}, \quad (\text{A5})$$

where  $\mathbf{V} = (U, V)$  is the spatially uniform horizontal wind vector, and  $\hat{h}$  is the Fourier transform of the terrain elevation. In accordance with the polarization relations of internal gravity waves (cf. Eqs. (5) and (6) in Xu et al., 2017b), the horizontal velocity in spectral space is

$$\hat{u} = i \frac{k}{K^2} \frac{\partial \hat{w}}{\partial z} = -\frac{k}{K} \frac{N}{Uk+Vl} \hat{w}, \quad (\text{A6})$$

$$\hat{v} = i \frac{l}{K^2} \frac{\partial \hat{w}}{\partial z} = -\frac{l}{K} \frac{N}{Uk+Vl} \hat{w}. \quad (\text{A7})$$



576 Substituting Eqs. (A5)-(A7) into (A4) yields

$$577 \quad \tau_0 = 4\pi^2 \rho_0 N \int_{-\infty}^{+\infty} \int_{-\infty}^{+\infty} \frac{\mathbf{K}}{K} (Uk + Vl) |\hat{h}|^2 dk dl. \quad (\text{A8})$$

578 For simplicity, polar coordinates are introduced, i.e.,  $\mathbf{K} = K(\cos\varphi, \sin\varphi)$  with  $K$  being the  
579 magnitude of the horizontal wavenumber vector, such that the above equation can be rewritten as

$$580 \quad \tau_0 = 8\pi^2 \rho_0 N |V_0| \int_{-\pi/2}^{+\pi/2} \int_0^\infty (\cos\varphi, \sin\varphi) \cos(\varphi - \psi_0) |\hat{h}|^2 K^2 dK d\varphi, \quad (\text{A9})$$

581 where  $|V_0|$  and  $\psi_0$  are the speed and direction of the horizontal wind at the surface, and  $\varphi$  is the  
582 azimuthal direction of the horizontal wavenumber vector.

583 For the elliptical bell-shaped mountain given by Eq. (1), the Fourier transform is

$$584 \quad \hat{h}(K, \varphi) = \frac{h_m ab}{2\pi} e^{-Kb\sqrt{\gamma^2 \cos^2 \varphi + \sin^2 \varphi}}, \quad (\text{A10})$$

585 where  $\gamma = \frac{a}{b}$  is the horizontal aspect ratio of the mountain. Substituting Eq. (A10) into Eq. (A9)  
586 results in

$$587 \quad \tau_0 = 2\rho_0 N |V_0| (h_m ab)^2 \int_{-\pi/2}^{+\pi/2} (\cos\varphi, \sin\varphi) \cos(\varphi - \psi_0) G(\varphi) d\varphi, \quad (\text{A11})$$

588 where

$$589 \quad G(\varphi) = \int_0^\infty e^{-2Kb\sqrt{\gamma^2 \cos^2 \varphi + \sin^2 \varphi}} K^2 dK = 4b^{-3} (\gamma^2 \cos^2 \varphi + \sin^2 \varphi)^{-\frac{3}{2}}, \quad (\text{A12})$$

590 with the latter equality in Eq. (A12) being obtained from  $\int_0^\infty e^{-qx} x^2 dx = 2q^{-3}$  (Gradshteyn and  
591 Ryzhik 2007). Finally, the WMF at the surface takes the form

$$592 \quad \tau_0 = 0.5\rho_0 N |V_0| h_m^2 a \gamma \int_{-\pi/2}^{+\pi/2} (\cos\varphi, \sin\varphi) \cos(\varphi - \psi_0) [\gamma^2 \cos^2 \varphi + \sin^2 \varphi]^{-\frac{3}{2}} d\varphi. \quad (\text{A13})$$

593 Note that the foregoing derivation was performed in a coordinate system with an arbitrary  
594 orientation up to Eq. (A9), but from Eq. (A10) to (A13) (which is identical to Eq. (2)), it was  
595 assumed that the principal axes of the elliptical mountain (which are by design chosen to be  
596 aligned with the incoming wind) are in the  $x$  and  $y$  directions respectively. In the general case of

597 an incoming wind and mountain that are oblique relative to the zonal-meridional directions (used  
598 in WRF), the transformation from one coordinate system to the other may be made  
599 straightforwardly by applying an appropriate horizontal rotation.

## References

- Alexander, M. J., and H. Teitelbaum, 2011: Three-dimensional properties of Andes mountain waves observed by satellite: A case study, *J. Geophys. Res. Atmos.*, **116**, D23110, <https://doi.org/10.1029/2011JD016151>.
- Alexander, M. J., and coauthors, 2010: Recent developments in gravity-wave effects in climate models and the global distribution of gravity-wave momentum flux from observations and models. *Quart. J. Roy. Meteor. Soc.*, **136**, 1103–1124. <https://doi.org/10.1002/qj.637>.
- Andrews, D. G., J. R. Holton, and C. B. Leovy, 1987: Middle Atmosphere Dynamics. Academic Press, 489 pp.
- Beljaars, A. C. M., 1994: The parameterization of surface fluxes in large-scale models under free convection. *Quart. J. Roy. Meteor. Soc.*, **121**, 255–270, <https://doi.org/10.1002/qj.49712152203>.
- Booker, J. R., and F. P. Bretherton, 1967: The critical layer for internal gravity waves in a shear flow, *J. Fluid Mech.*, **27**, 513–539, <https://doi.org/10.1017/S0022112067000515>.
- Broad, A. S., 1995: Linear theory of momentum fluxes in 3-D flows with turning of the mean wind with height, *Quart. J. Roy. Meteor. Soc.*, **121**, 1891–1902, <https://doi.org/10.1002/qj.49712152806>.
- Calvo, N., Garcia, R. R., and D. E. Kinnison, 2017: Revisiting Southern Hemisphere polar stratospheric temperature trends in WACCM: The role of dynamical forcing. *Geophys. Res. Lett.*, **44** 3402–3410, <https://doi.org/10.1002/2017GL072792>.

620 Choi, H.-J., and S.-Y. Hong, 2015: An updated subgrid orographic parameterization for global  
621 atmospheric forecast models, *J. Geophys. Res. Atmos.*, **120**, 12,445–12,457,  
622 <https://doi.org/10.1002/2015JD024230>.

623 Choi, H.-J., Choi, S.-J., Koo, M.-S., Kim, J.-E., Kwon, Y. C., and S.-Y. Hong, 2017: Effects of  
624 parameterized orographic drag on weather forecasting and simulated climatology over  
625 East Asia during boreal summer. *J. Geophys. Res. Atmos.*, **122**, 10669–  
626 10678, <https://doi.org/10.1002/2017JD026696>.

627 Cohen, N. Y., Edwin P. G., and B. Oliver, 2013: Compensation between resolved and unresolved  
628 wave driving in the stratosphere: Implications for downward control. *J. Atmos.*  
629 *Sci.*, **70**, 3780–3798, <https://doi.org/10.1175/JAS-D-12-0346.1>.

630 Eckermann, S. D., J. Ma, and D. Broutman, 2015: Effects of horizontal geometrical spreading on  
631 the parameterization of orographic gravity wave drag. Part I: Numerical transform  
632 solutions, *J. Atmos. Sci.*, **72**, 2330–2347, <https://doi.org/10.1175/JAS-D-14-0147.1>.

633 Edmon, H. J., B. J. Hoskins, and M. E. McIntyre, 1980: Eliassen-Palm cross sections for the  
634 troposphere. *J. Atmos. Sci.*, **37**, 2600–2616, [http://dx.doi.org/10.1175/1520-](http://dx.doi.org/10.1175/1520-0469(1980)037<2600:EPCSFT>2.0.CO;2)  
635 [0469\(1980\)037<2600:EPCSFT>2.0.CO;2](http://dx.doi.org/10.1175/1520-0469(1980)037<2600:EPCSFT>2.0.CO;2).

636 Ehard, B., and Coauthors, 2017: Vertical propagation of large-amplitude mountain waves in the  
637 vicinity of the polar night jet, *J. Geophys. Res. Atmos.*, **122**, 1423–1436,  
638 <https://doi.org/10.1002/2016JD025621>.

639 Eliassen, A., and E. Palm, 1961: On the transfer of energy in stationary mountain  
640 waves. *Geofysiske Publikasjoner*, **22**, 1–23, <https://doi.org/10.1002/qj.49707934103>.

- Fritts, D. C., and M. J. Alexander, 2003: Gravity wave dynamics and effects in the middle atmosphere, *Rev. Geophys.*, **41**, 1003, <https://doi.org/10.1029/2001RG000106>.
- Garcia, R. R., Smith, A. K., Kinnison, D. E., de la Cámara, A., and D. J. Murphy, 2017: Modification of the gravity wave parameterization in the Whole Atmosphere Community Climate Model: Motivation and results. *J. Atmos. Sci.*, **74**, 275–291, <https://doi.org/10.1175/JAS-D-16-0104.1>
- Geller, M., Alexander, M. J., Love, P., Bacmeister, J., Ern, M., Hertzog, A., Manzini, E., Preusse, P., Sato, K., Scaife, A., and Zhou, T., 2013: A Comparison between gravity wave momentum fluxes in observations and climate models. *J. Climate*, **26**, 6383–6405, <https://doi.org/10.1175/JCLI-D-12-00545.1>
- Gradshteyn, I. S., and I. M. Ryzhik, 2007: Table of Integrals, Series, and Products. Academic Press, Seventh Edition, 1171 pp.
- Haynes, P. H., C. J. Marks, M. E. McIntyre, T. G. Shepherd, and K. P. Shine, 1991: On the “downward control” of extratropical diabatic circulations by eddy-induced mean zonal forces, *J. Atmos. Sci.*, **48**, 651–678, [https://doi.org/10.1175/1520-0469\(1991\)048<0651:OTCOED>2.0.CO;2](https://doi.org/10.1175/1520-0469(1991)048<0651:OTCOED>2.0.CO;2).
- Hindley, N. P., Wright, C. J., Smith, N. D., and Mitchell, N. J., 2015: The southern stratospheric gravity wave hot spot: individual waves and their momentum fluxes measured by COSMIC GPS-RO, *Atmos. Chem. Phys.*, **15**, 7797–7818, <https://doi.org/10.5194/acp-15-7797-2015>.

662 Hong, S.-Y., J. Dudhia, and S. Chen, 2004: A revised approach to ice microphysical processes  
 663 for the bulk parameterization of clouds and precipitation. *Mon. Wea. Rev.*, **132**, 103–120,  
 664 [https://doi.org/10.1175/1520-0493\(2004\)132<0103:ARATIM>2.0.CO;2](https://doi.org/10.1175/1520-0493(2004)132<0103:ARATIM>2.0.CO;2).

665 Hong, S.- Y., Y. Noh, and J. Dudhia, 2006: A new vertical diffusion package with an explicit  
 666 treatment of entrainment processes. *Mon. Wea. Rev.*, **134**, 2318–2341,  
 667 <https://doi.org/10.1175/MWR3199.1>.

668 Hong, S.-Y., Choi, J., Chang, E.-C., Park, H., and Y.-J. Kim, 2008: Lower-tropospheric  
 669 enhancement of gravity wave drag in a global spectral atmospheric forecast model. *Wea.*  
 670 *Forecasting*, **23**, 523–531, <https://doi.org/10.1175/2007waf2007030.1>.

671 Hurrell, J. W., and Coauthors, 2013: The Community Earth System Model: A framework for  
 672 collaborative research. *Bull. Amer. Meteor. Soc.*, **94**, 1339–1360,  
 673 <https://doi.org/10.1175/BAMS-D-12-00121.1>

674 Iacono, M. J., J. S. Delamere, E. J. Mlawer, M. W. Shephard, S. A. Clough, and W. D. Collins,  
 675 2008: Radiative forcing by long-lived greenhouse gases: Calculations with the AER  
 676 radiative transfer models. *J. Geophys. Res. Atmos.*, **113**, D13103,  
 677 <https://doi.org/10.1029/2008JD009944>.

678 Kalisch, S., Preusse, P., Ern, M., Eckermann, S. D., and M. Riese, 2014: Differences in gravity  
 679 wave drag between realistic oblique and assumed vertical propagation. *J. Geophys. Res.*  
 680 *Atmos.*, **119**, 10081–10099, <https://doi.org/10.1002/2014JD021779>.

681 Kim, Y.-J., and A. Arakawa, 1995: Improvement of orographic gravity wave parameterization  
 682 using a mesoscale gravity wave model. *J. Atmos. Sci.*, **52**, 1875–  
 683 1902, [https://doi.org/10.1175/1520-0469\(1995\)052<1875:IOOGWP>2.0.CO;2](https://doi.org/10.1175/1520-0469(1995)052<1875:IOOGWP>2.0.CO;2).

684 Kim, Y. -J., and J. D. Doyle, 2005: Extension of an orographic-drag parameterization scheme to  
685 incorporate orographic anisotropy and flow blocking, *Quart. J. Roy. Meteor. Soc.*, **131**,  
686 1893–1921, <https://doi.org/10.1256/qj.04.160>.

687 Kim, Y.-J., and S.-Y. Hong, 2009: Interaction between the orography-induced gravity wave drag  
688 and boundary layer processes in a global atmospheric model, *Geophys. Res. Lett.*, **36**,  
689 L12809, <https://doi.org/10.1029/2008GL037146>.

690 Kim, Y. -J., S. D. Eckermann, and H. Y. Chun, 2003: An overview of the past, present and future  
691 of gravity-wave drag parametrization for numerical climate and weather prediction  
692 models. *Atmos.– Ocean*, **41**, 65–98, <https://doi.org/10.3137/ao.410105>.

693 Kruse, C. G., R. B. Smith, and S. D. Eckermann, 2016: The mid-latitude lower-stratospheric  
694 mountain wave “valve layer”, *J. Atmos. Sci.*, **73**, 5081–5100,  
695 <https://doi.org/10.1175/JAS-D-16-0173.1>.

696 Lindzen, R. S., 1981: Turbulence and stress owing to gravity wave and tidal breakdown. *J.*  
697 *Geophys. Res. Atmos.*, **86**, 9707–9714, <https://doi.org/10.1029/JC086iC10p09707>.

698 Lott, F., 1999: Alleviation of stationary biases in a GCM through a mountain drag  
699 parametrization scheme and a simple representation of mountain lift forces. *Mon. Wea.*  
700 *Rev.*, **127**, 788-801, [https://doi.org/10.1175/1520-](https://doi.org/10.1175/1520-0493(1999)127<0788:AOSBIA>2.0.CO;2)  
701 [0493\(1999\)127<0788:AOSBIA>2.0.CO;2](https://doi.org/10.1175/1520-0493(1999)127<0788:AOSBIA>2.0.CO;2)

702 Lott, F., and M. Miller, 1997: A new sub-grid orographic drag parameterization: Its formulation  
703 and testing, *Quart. J. Roy. Meteor. Soc.*, **123**, 101–127,  
704 <https://doi.org/10.1002/qj.49712353704>.

705 Martin, A., and F. Lott, 2007: Synoptic responses to mountain gravity waves encountering  
 706 directional critical levels. *J. Atmos. Sci.*, **64**, 828-848, <https://doi.org/10.1175/JAS3873.1>

707 McFarlane, N. A., 1987: The effect of orographically excited gravity wave drag on the general  
 708 circulation of the lower stratosphere and troposphere. *J. Atmos. Sci.*, **44**, 1775–  
 709 1800, [https://doi.org/10.1175/1520-0469\(1987\)044<1775:teooeg>2.0.co;2](https://doi.org/10.1175/1520-0469(1987)044<1775:teooeg>2.0.co;2).

710 McLandress, C., and T. G. Shepherd, 2009: Simulated anthropogenic changes in the Brewer-  
 711 Dobson circulation, including its extension to high latitudes, *J. Climate*, **22**, 1516–1540,  
 712 <https://doi.org/10.1175/2008JCLI2679.1>.

713 McLandress, C., T. G. Shepherd, S. Polavaparu, and S. R. Beagley, 2012: Is missing orographic  
 714 gravity wave drag near 60°S the cause of the stratospheric zonal wind biases in  
 715 chemistry–climate models? *J. Atmos. Sci.*, **69**, 802–818, [https://doi.org/10.1175/JAS-D-](https://doi.org/10.1175/JAS-D-11-0159.1)  
 716 [11-0159.1](https://doi.org/10.1175/JAS-D-11-0159.1).

717 Palmer, T. N., G. J. Shutts, and R. Swinbank, 1986: Alleviation of systematic westerly bias in  
 718 general circulation and numerical weather prediction models through an orographic  
 719 gravity wave drag parameterization. *Quart. J. Roy. Meteor. Soc.*, **112**, 1001–1039,  
 720 <https://doi.org/10.1002/qj.49711247406>.

721 Phillips, D. S., 1984: Analytical surface pressure and drag for linear hydrostatic flow over three-  
 722 dimensional elliptical mountains, *J. Atmos. Sci.*, **41**, 1073–1084,  
 723 [https://doi.org/10.1175/1520-0469\(1984\)041,1073:ASPADF.2.0.CO;2](https://doi.org/10.1175/1520-0469(1984)041,1073:ASPADF.2.0.CO;2).

724 Pithan, F., Shepherd, T. G., Zappa, G., and I. Sandu, 2016: Missing orographic drag leads to  
 725 climate model biases in jet streams, blocking and storm tracks. *Geophys. Res.*  
 726 *Lett.*, **43**, 7231–7240, <https://doi.org/10.1002/2016GL069551>.



727 Pulido, M., and C. Rodas, 2011: A higher-order ray approximation applied to orographic waves:  
 728 Gaussian beam approximation, *J. Atmos. Sci.*, **68**, 46–60,  
 729 <https://doi.org/10.1175/2010JAS3468.1>.

730 Pulido, M., and J. Thuburn, 2005: Gravity-wave drag estimation from global analyses using  
 731 variational data assimilation principles. I: Theory and implementation. *Quart. J. Roy.*  
 732 *Meteor. Soc.*, **131**, 1821–1840, <https://doi.org/10.1256/qj.04.116>.

733 Richardson, M. I., A. D. Toigo, and C. E. Newman, 2007: Planet WRF: A General Purpose,  
 734 Local to Global Numerical Model for Planetary Atmosphere and Climate Dynamics, *J.*  
 735 *Geophys. Res. Atmos.*, **112**, E09001, <https://doi.org/10.1029/2006JE002825>.

736 Sandu, I., P. Bechtold, A. Beljaars, A. Bozzo, F. Pithan, T. G. Shepherd, and A. Zadra, 2016:  
 737 Impacts of parameterized orographic drag on the Northern Hemisphere winter circulation,  
 738 *J. Adv. Model. Earth Syst.*, **8**, 196–211, <https://doi.org/10.1002/2015MS000564>.

739 Scheffler, G., and M. Pulido, 2017: Estimation of gravity-wave parameters to alleviate the delay  
 740 in the Antarctic vortex breakup in general circulation models. *Quart. J. Roy. Meteor.*  
 741 *Soc.*, **143**, 2157–2167, <https://doi.org/10.1002/qj.3074>.

742 Scinocca, J. F., and N. A. McFarlane, 2000: The parametrization of drag induced by stratified  
 743 flow over anisotropic orography, *Quart. J. Roy. Meteor. Soc.*, **126**, 2353–2393,  
 744 <https://doi.org/10.1002/qj.49712656802>.

745 Shepherd, T. G., 2014: Atmospheric circulation as a source of uncertainty in climate change  
 746 projections, *Nat. Geosci.*, **7**, 703–708, <https://doi.org/10.1038/ngeo2253>.

747 Shin, H. H., S.-Y. Hong, J. Dudhia, and Y.-J. Kim, 2010: Orography-induced gravity wave drag  
 748 parameterization in the global WRF: Implementation and sensitivity to shortwave  
 749 radiation schemes. *Adv. Meteor.*, **2010**, 959014, <https://doi.org/10.1155/2010/959014>.

750 Shutts, G., 1995: Gravity-wave drag parameterization over complex terrain: The effect of  
 751 critical-level absorption in directional wind-shear. *Quart. J. Roy. Meteor. Soc.*, **121**,  
 752 1005–1021, <https://doi.org/10.1002/qj.49712152504>.

753 Sigmond, M., and J. F. Scinocca, 2010: The influence of the basic state on the Northern  
 754 Hemisphere circulation response to climate change. *J. Climate*, **23**, 1434–  
 755 1446, <https://doi.org/10.1175/2009JCLI3167.1>

756 Sigmond, M., and T. G. Shepherd, 2014: Compensation between resolved wave driving and  
 757 parameterized orographic gravity wave driving of the Brewer–Dobson circulation and its  
 758 response to climate change. *J. Climate*, **27**, 5601–5610, [https://doi.org/10.1175/JCLI-D-](https://doi.org/10.1175/JCLI-D-13-00644.1)  
 759 13-00644.1.

760 Smith, A. K., N. M. Pedatella, D. R. Marsh, and T. Matsuo, 2017: On the dynamical control of  
 761 the mesosphere–lower thermosphere by the lower and middle atmosphere. *J. Atmos. Sci.*,  
 762 **74**, 933–947, <https://doi.org/10.1175/JAS-D-16-0226.1>

763 Teixeira, M. A. C., and P. M. A. Miranda, 2006: A linear model of gravity wave drag for  
 764 hydrostatic sheared flow over elliptical mountains. *Quart. J. Roy. Meteor.*  
 765 *Soc.*, **132**, 2439–2458, <https://doi.org/10.1256/qj.05.220>.

766 Teixeira, M. A. C., and P. M. A. Miranda, 2009: On the momentum fluxes associated with  
 767 mountain waves in directionally sheared flows, *J. Atmos. Sci.*, **66**, 3419–3433,  
 768 <https://doi.org/10.1175/2009JAS3065.1>.

769 Teixeira, M. A. C., and C. L. Yu, 2014: The gravity wave momentum flux in hydrostatic flow  
770 with directional shear over elliptical mountains. *European Journal of Mechanics &*  
771 *Fluids B: Fluids*, **47**, 16-31, <https://doi.org/10.1016/j.euromechflu.2014.02.004>.

772 Tewari, M., and coauthors, 2004: Implementation and verification of the unified NOAA land  
773 surface model in the WRF model. 20th conference on weather analysis and  
774 forecasting/16th conference on numerical weather prediction, pp. 11–15.

775 van Niekerk, A., Scinocca, J. F., and T. G. Shepherd, 2017: The modulation of stationary waves,  
776 and their response to climate change, by parameterized orographic drag. *J. Atmos.*  
777 *Sci.*, **74**, 2557–2574, <https://doi.org/10.1175/JAS-D-17-0085.1>.

778 Webster, S., Brown, A. R., Cameron, D. R., and C. P. Jones, 2003: Improvements to the  
779 representation of orography in the met office unified model. *Quart. J. Roy. Meteor.*  
780 *Soc*, **129**, 1989–2010, <https://doi.org/10.1256/qj.02.133>.

781 Xu, X., Y. Wang, and M. Xue, 2012: Momentum flux and flux divergence of gravity waves in  
782 directional shear flows over three-dimensional mountains, *J. Atmos. Sci.*, **69**, 3733–3744,  
783 <https://doi.org/10.1175/JAS-D-12-044.1>.

784 Xu, X., Xue, M., and Y. Wang, 2013: Gravity wave momentum flux in directional shear flows  
785 over three-dimensional mountains: Linear and nonlinear numerical solutions as compared  
786 to linear analytical solutions. *J. Geophys. Res. Atmos*, **118**, 7670–7681,  
787 <https://doi.org/10.1002/jgrd.50471>.

788 Xu, X., J. Song, Y. Wang, and M. Xue, 2017a: Quantifying the Effect of Horizontal Propagation  
789 of Three-Dimensional Mountain Waves on the Wave Momentum Flux Using Gaussian

790 Beam Approximation, *J. Atmos. Sci.*, **74**, 1783–1798, <https://doi.org/10.1175/JAS-D-16->  
791 0275.1.

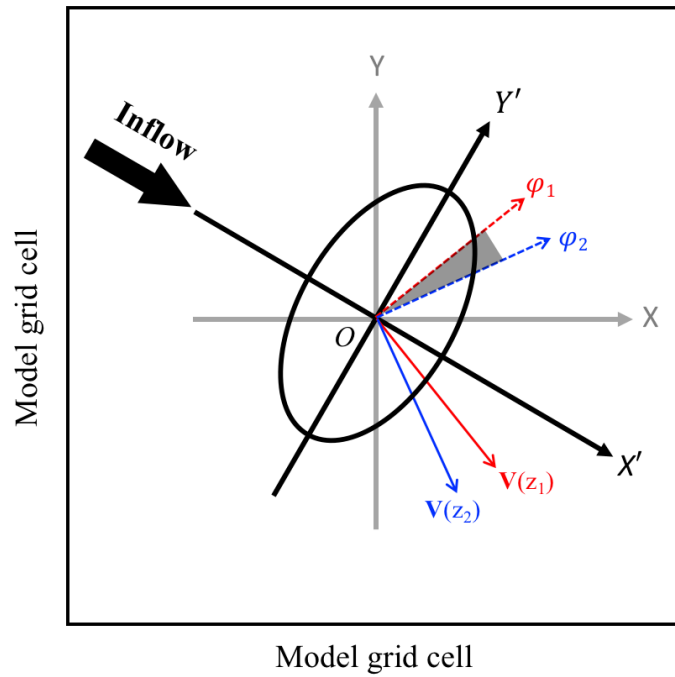
792 Xu, X., Shu, S., and Y. Wang, 2017b: Another look on the structure of mountain waves: A  
793 spectral perspective. *Atmos. Res.*, **191**, 156–163,  
794 <https://doi.org/10.1016/j.atmosres.2017.03.015>.

795 Xu, X., Y. Tang, Y. Wang, and M. Xue, 2018: Directional absorption of mountain waves and its  
796 influence on the wave momentum transport in the Northern Hemisphere. *J. Geophys. Res.*  
797 *Atmos.*, **123**, 2640–2654, <https://doi.org/10.1002/2017JD027968>.

798 Zhang, C., Y. Wang, and K. Hamilton, 2011: Improved representation of boundary layer clouds  
799 over the southeast pacific in ARW–WRF using a modified Tiedtke cumulus  
800 parameterization scheme. *Mon. Wea. Rev.*, **139**, 3489–3513,  
801 <https://doi.org/10.1175/MWR-D-10-05091.1>.

802 Zhong, S., and Z. Chen, 2015: Improved wind and precipitation forecasts over South China using  
803 a modified orographic drag parameterization scheme. *J. Meteor. Res.*, **29**, 132–  
804 143, <https://doi.org/10.1007/s13351-014-4934-1>.  
805

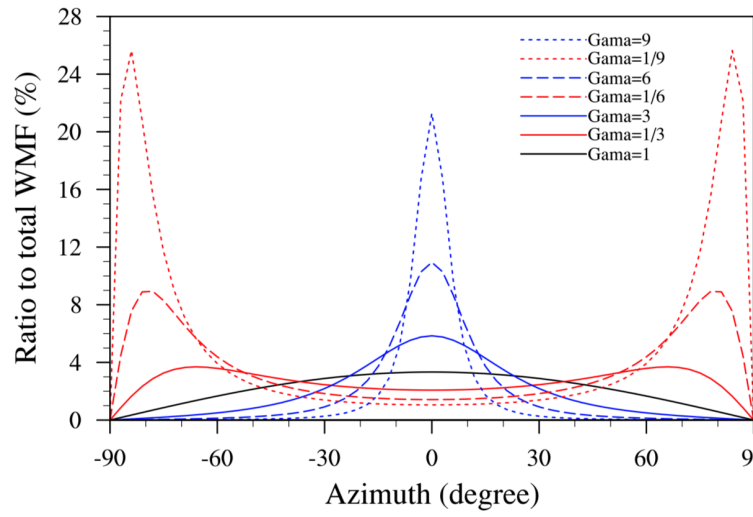
806



807  
808  
809  
810  
811  
812  
813  
814

Fig. 1. Schematic of elliptical SSO within a model grid cell. The principal axis of the SSO is (by design) along the direction of low-level inflow. Solid red and blue arrows indicate the horizontal winds at heights  $z_1$  and  $z_2$  respectively. Dashed red and blue arrows are perpendicular to their solid counterparts. Due to rotation of the horizontal wind with height, the wave components between the azimuths  $\varphi_1$  and  $\varphi_2$  (grey shading) are selectively absorbed.

815



816

817

818

819

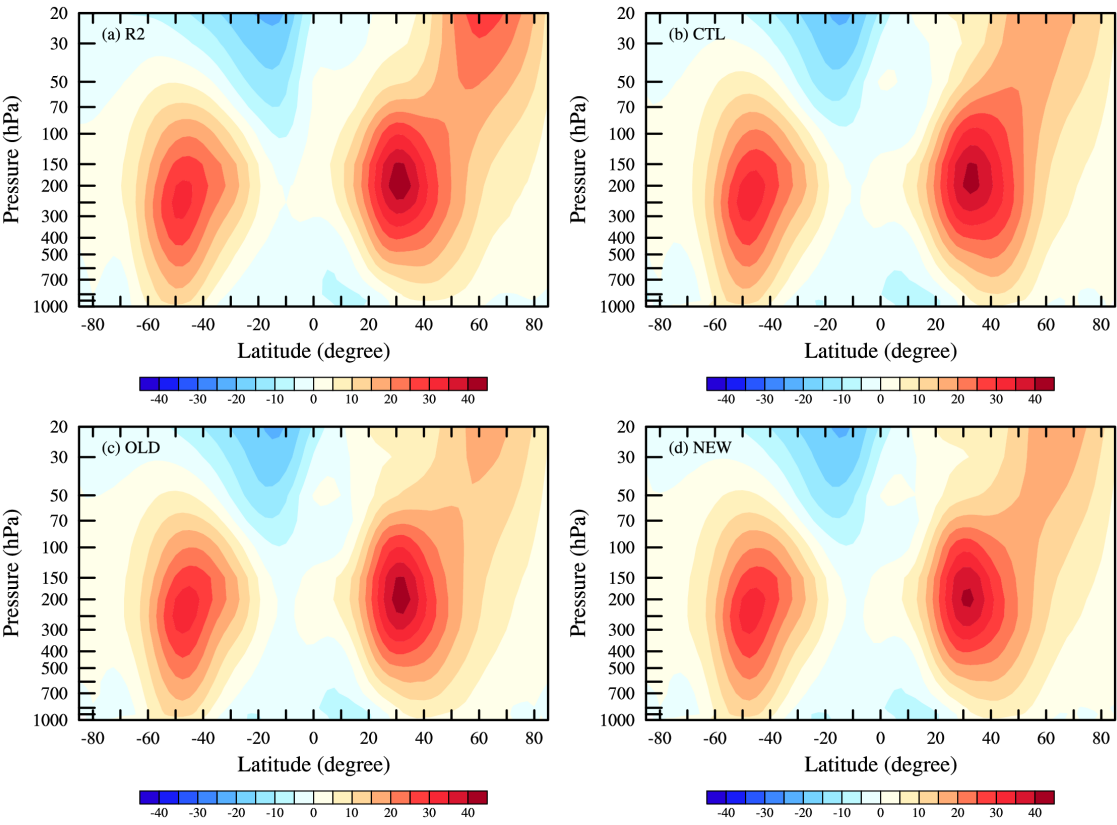
820

821

822

Fig. 2. Distribution of WMF about the orientation of the horizontal wave number for gravity waves forced by elliptical mountains of different horizontal aspect ratios of  $\gamma = 1$  (black),  $1/3$  (solid red),  $3$  (solid blue),  $1/6$  (dashed red),  $6$  (dashed blue),  $1/9$  (dotted red), and  $9$  (dotted blue).

823



824

825

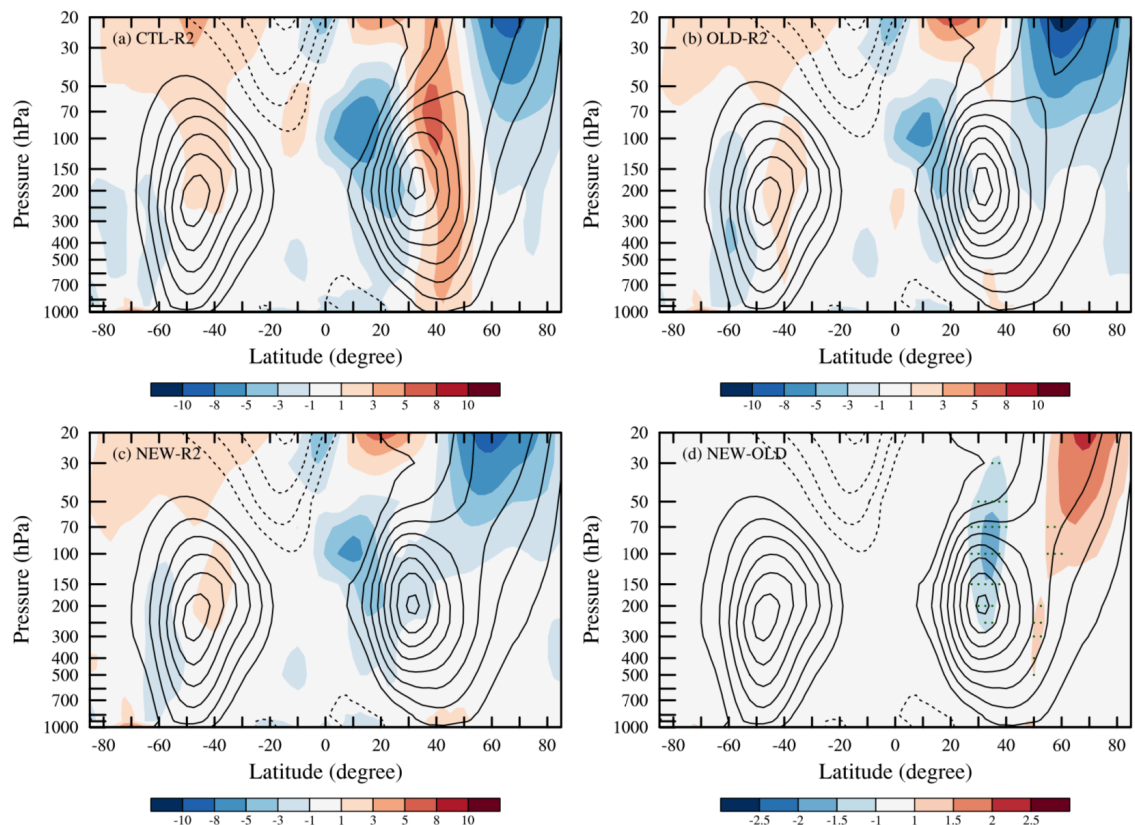
826

827

828

829

Fig. 3. Zonal-mean zonal winds (units:  $\text{m s}^{-1}$ ) in January averaged from 2013 to 2018 from the (a) NCEP Reanalysis (R2) and global WRF simulations of the (b) CTL, (c) OLD, and (d) NEW experiments.



831

832

833

834

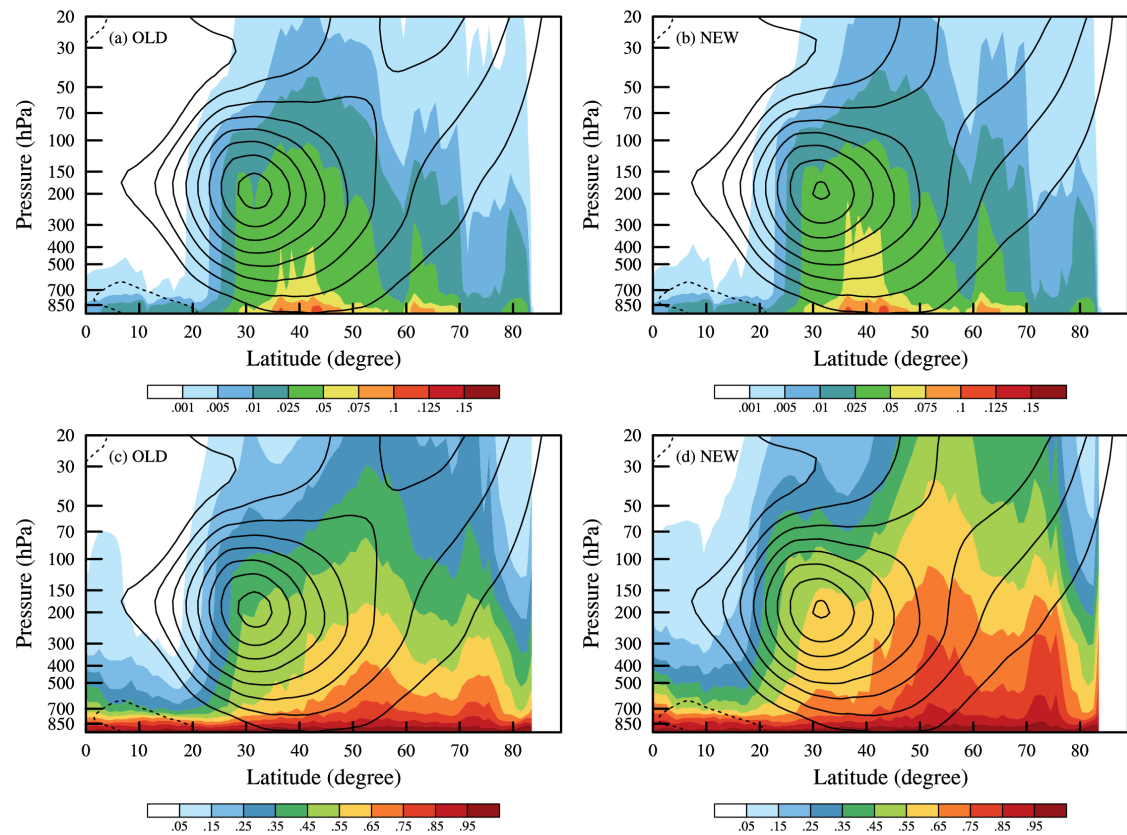
835

836

837

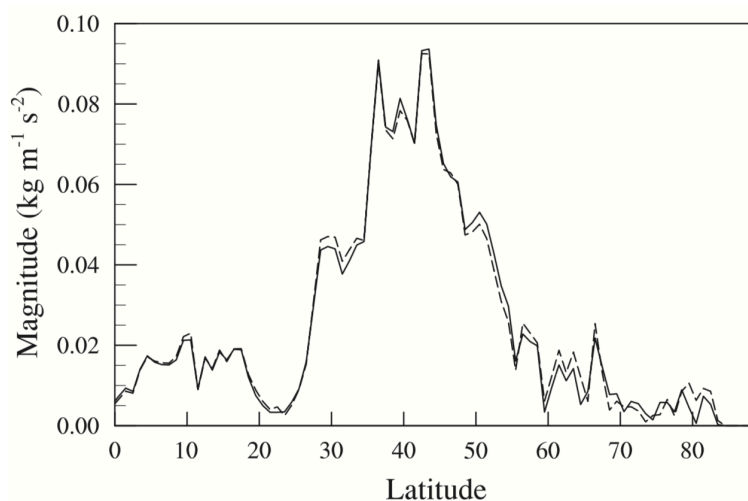
Fig. 4. Zonal wind difference (shading, units:  $\text{m s}^{-1}$ ) between the NCEP Reanalysis and WRF simulations averaged for January of 2013-2018. (a) CTL, (b) OLD, and (c) NEW. (d) Difference between the zonal winds in OLD and NEW. Contour lines are the corresponding zonal-mean zonal winds (units:  $\text{m s}^{-1}$ ). Statistical significance at the 99% level using the student  $t$  test is indicated by green dots in (d).





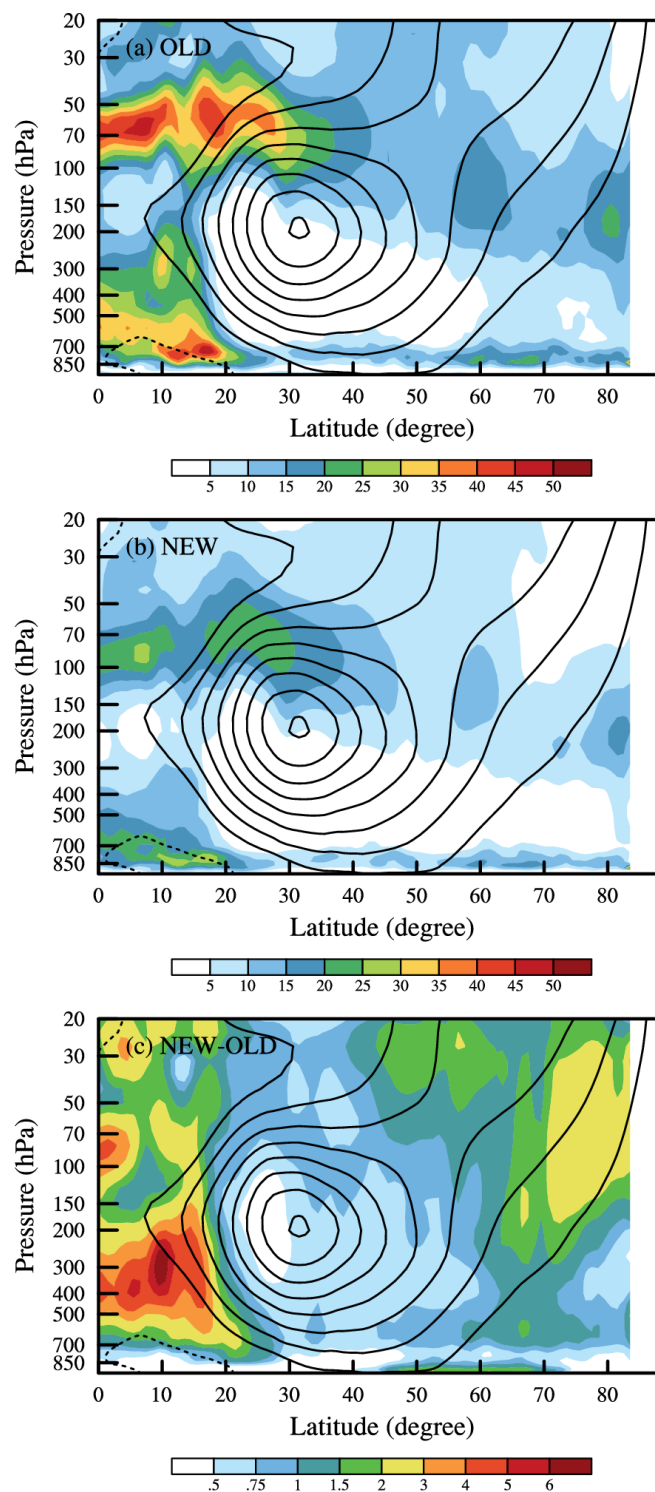
840 Fig. 5. Vertical distribution of zonal-mean WMF (shading, units:  $\text{kg m}^{-1} \text{s}^{-2}$ ) in the Northern  
841 Hemisphere averaged for January of 2013-2018 in the (a) OLD and (b) NEW experiment. (c) and  
842 (d) are similar to (a) and (b) but for the scaled WMF (units: %) normalized by surface WMF.  
843 Contours are the corresponding zonal-mean zonal winds (units:  $\text{m s}^{-1}$ ).  
844

845  
846



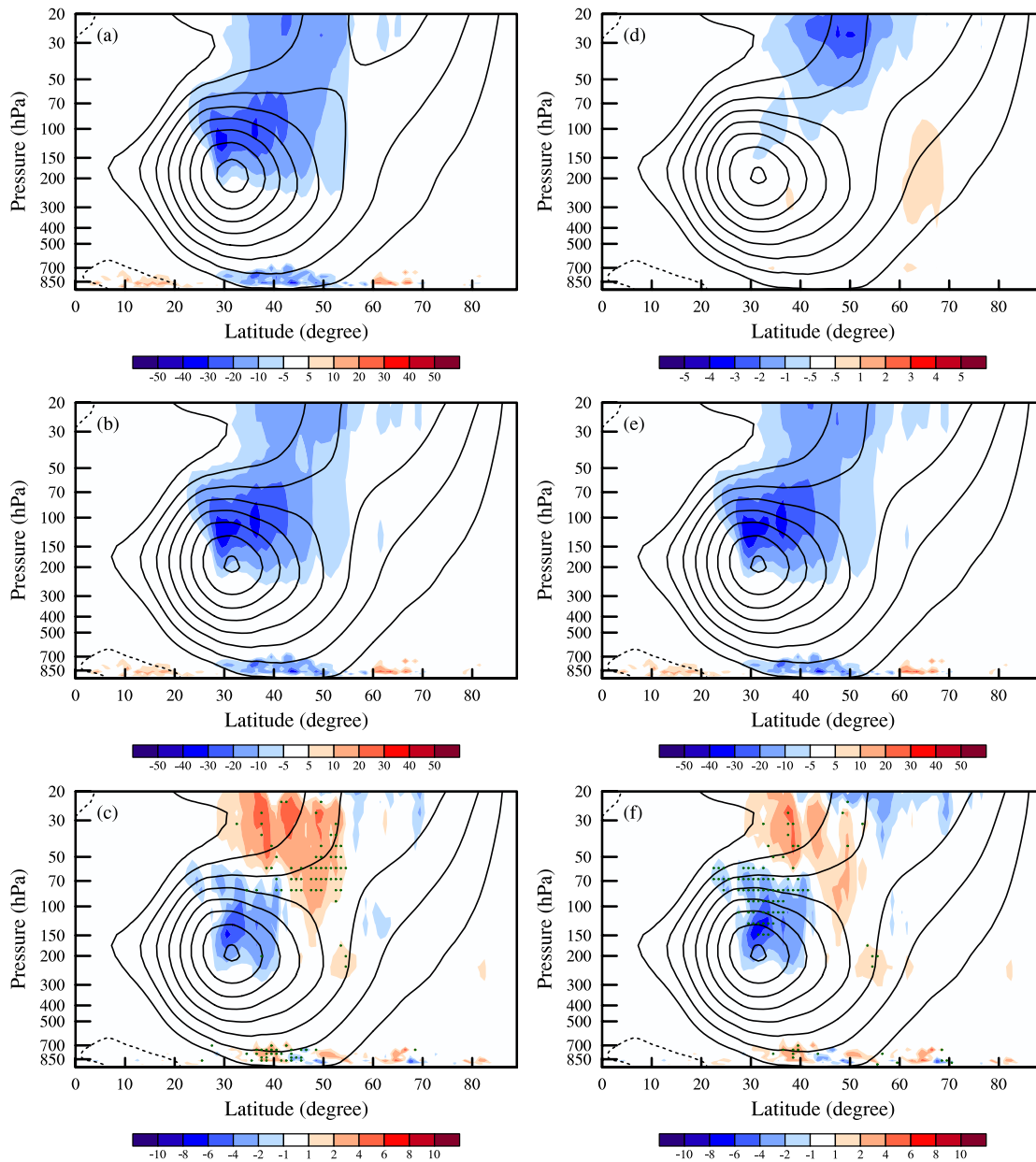
847  
848 Fig. 6. Zonal-mean column-integrated OGW forcing in the OLD (solid) and NEW (dashed)  
849 experiments in the Northern Hemisphere averaged for January 2013-2018.  
850

851  
852



854

855 Fig. 7. WMF attenuation (shading, units: %) due to wave breaking in the (a) OLD and (b) NEW  
 856 experiment in the Northern Hemisphere averaged for January 2013-2018. (c) is similar to (b) but  
 857 for the WMF attenuation due to directional absorption. Contours are the corresponding zonal-  
 858 mean zonal winds (units:  $\text{m s}^{-1}$ ).



860

861 Fig. 8. Vertical distribution of zonal-mean OGWD due to wave breaking (shading: units:  $\text{m s}^{-2}$ )  
 862 in the (a) OLD and (b) NEW experiment in the Northern Hemisphere averaged for January 2013-  
 863 2018, with their difference (NEW minus OLD) shown in (c). (d) is similar to (b) but for zonal-  
 864 mean OGWL due to directional absorption in the NEW experiment. (e) Sum of OGWD and  
 865 OGWL (i.e., total OGW forcing) in NEW. (f) Difference between the total OGW forcing in the  
 866 OLD and NEW experiment, i.e., (e)-(a). Contour lines are the corresponding zonal-mean zonal  
 867 winds (units:  $\text{m s}^{-1}$ ). Statistical significance at the 99% level using the student  $t$  test is indicated  
 868 by green dots in (c) and (f).

869

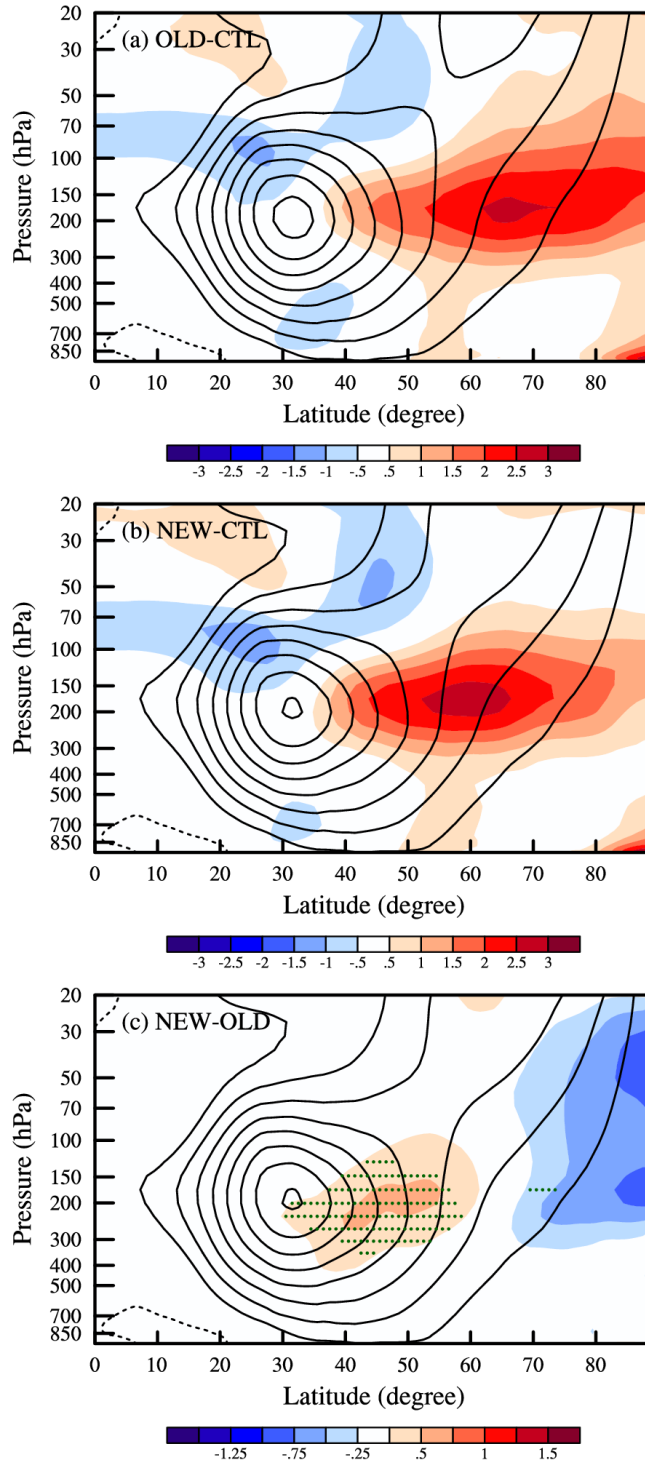
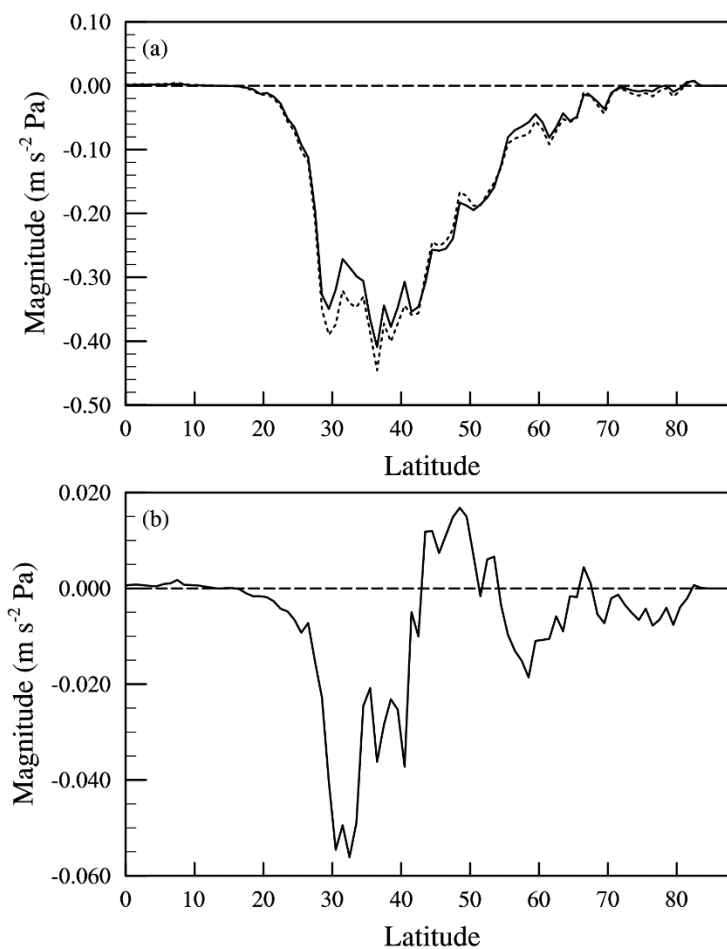


Fig. 9. Vertical distribution of zonal-mean temperature difference (shading, units: K) between (a) CTL and OLD (OLD minus CTL), (b) CTL and NEW (NEW minus CTL), and (c) OLD and NEW (NEW minus OLD) in the Northern Hemisphere averaged for January 2013-2018. Contour lines are the corresponding zonal-mean zonal winds (units:  $\text{m s}^{-1}$ ). Statistical significance at the 99% level using the student  $t$  test is indicated by green dots in (c)

876

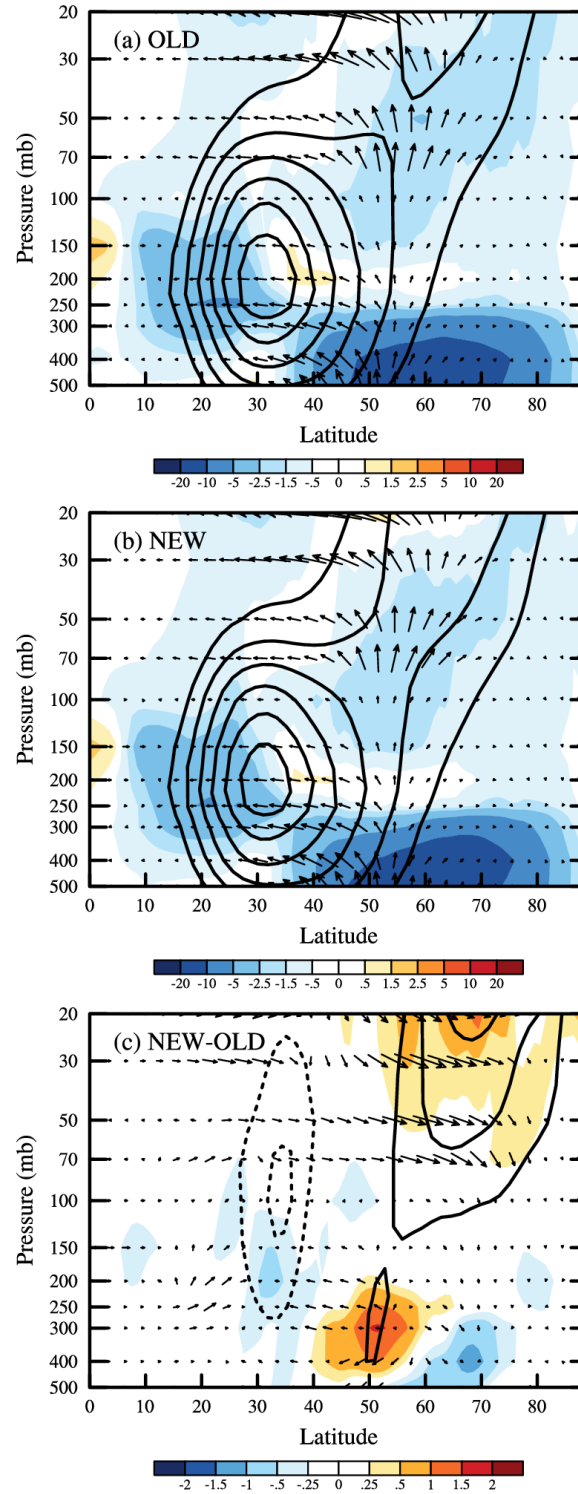


877

878 Fig. 10. Zonal-mean (a) OGW forcing integrated between 200 hPa and the model top (units:  $\text{m s}^{-2} \text{ Pa}$ ) in the OLD (solid) and NEW (dotted) experiment and (b) their difference (NEW minus  
879  
880 OLD) in the Northern Hemisphere averaged for January 2013-2018.

881

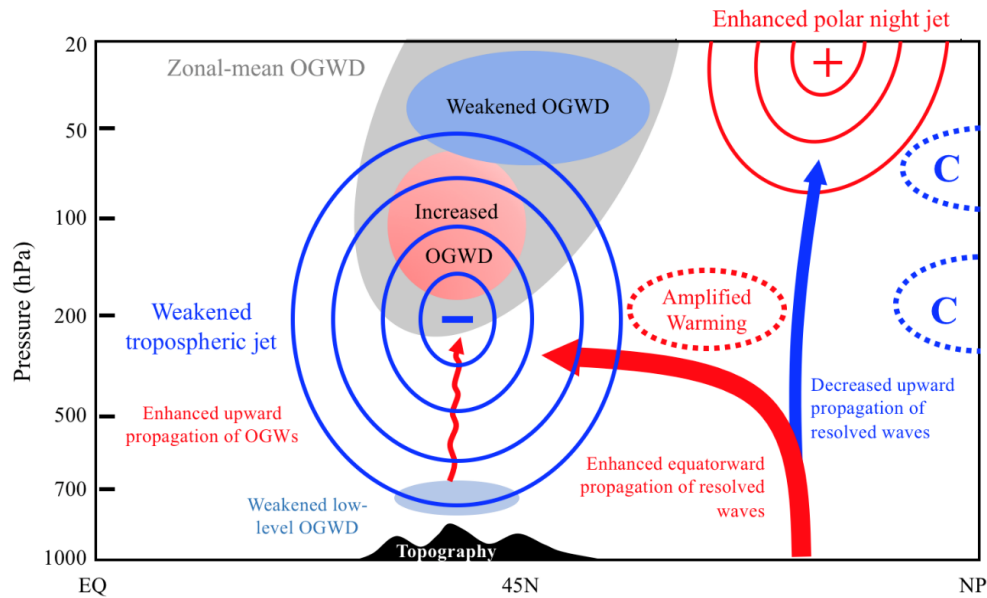
882



883

884 Fig. 11 Vertical distribution of zonal-mean EP flux (vectors) and acceleration (shading, units:  $\text{m s}^{-2}$ ) due to resolved waves in the Northern Hemisphere averaged for January 2013-2018 in the (a)  
 885 OLD and (b) NEW experiment. Contour lines are the corresponding zonal-mean zonal winds (units:  $\text{m s}^{-1}$ ). (c) Difference between (a) and (b) (b minus a). The EP flux above 100 hPa is  
 886  
 887  
 888 exaggerated by a factor of 5 for clarity.

889  
890

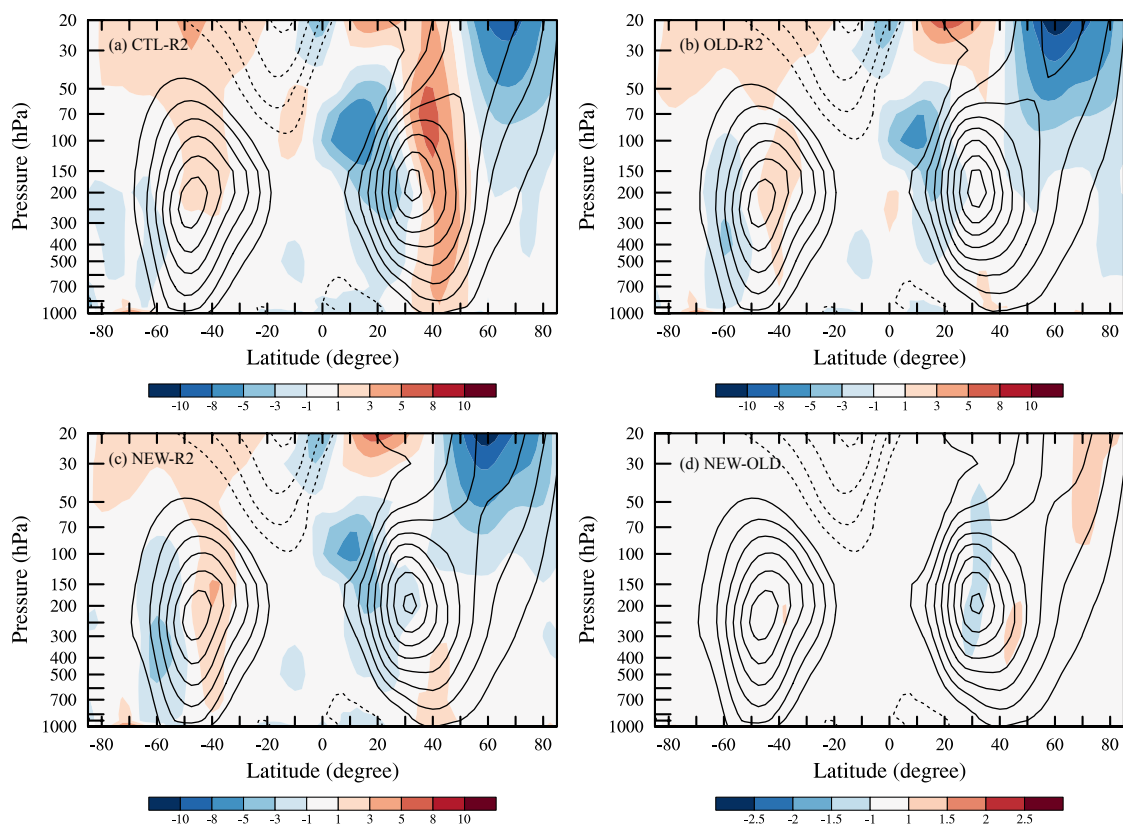


891  
892  
893  
894  
895  
896  
897  
898  
899  
900  
901

Fig. 12. Schematic illustration of the impact of directional absorption of OGWs on the large-scale atmospheric circulation in boreal winter. Solid blue and red contours in the midlatitude troposphere and high-latitude stratosphere denote the weakened tropospheric jet and enhanced stratospheric polar night jet, respectively. Dashed red and blue contours indicate increased and suppressed warming in the mid and high latitudes respectively. Grey shading represents the zonal mean OGWD, with blue (red) shadings denoting reduced (increased) OGWD in the lower troposphere and stratosphere (upper troposphere) of midlatitudes. The thick red arrow denotes enhanced equatorward propagation of resolved waves, whereas the thin blue arrow indicates decreased upward propagation of resolved waves into the stratosphere.



902

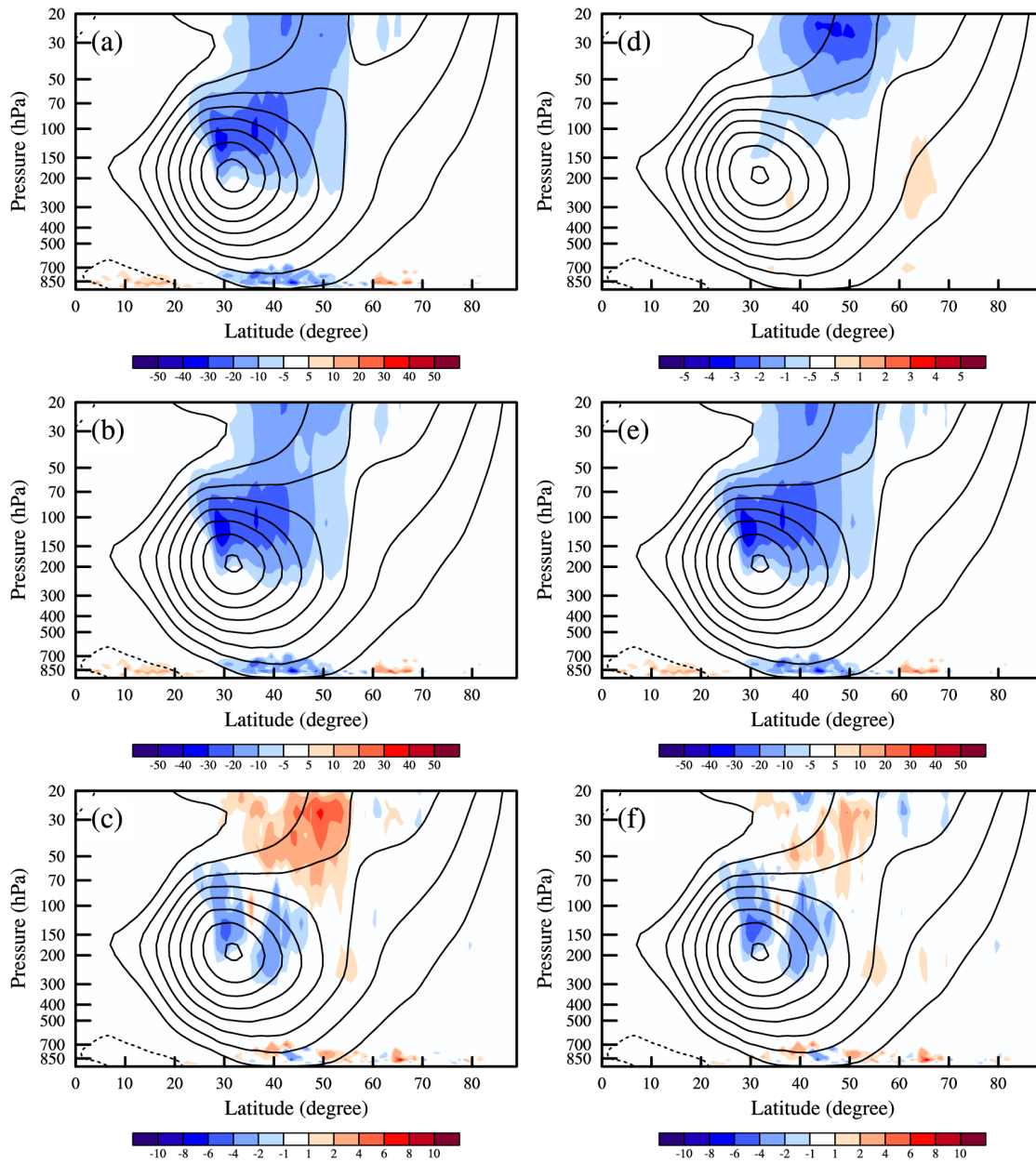


903

904 Fig. 13. Similar to Fig. 4 except for the “weak directional absorption” case (NEW1 experiment).

905

906  
907



908  
909  
910

Fig. 14. Similar to Fig. 8 except for the “weak directional absorption” case (NEW1 experiment).